Check for updates

JGR Solid Earth

RESEARCH ARTICLE
10.1029/2019JB019281

Special Section:
Creep on continental faults and subduction zones: Geophysics, geology, and mechanics

Volcano-Tectonic Interactions at Sabancaya Volcano, Peru: Eruptions, Magmatic Inflation, Moderate Earthquakes, and Fault Creep

Patricia MacQueen[1], Francisco Delgado[1,2], Kevin Reath[1], Matthew E. Pritchard[1], Marco Bagnardi[3,4], Pietro Milillo[3], Paul Lundgren[3], Orlando Macedo[5], Victor Aguilar[5], Mayra Ortega[6], Rosa Anccasi[6], Ivonne Alejandra Lazarte Zerpa[6,7], and Rafael Miranda[6]

[1]Department of Earth and Atmospheric Sciences,Cornell University, Ithaca, NY, USA, [2]Université de Paris, Institut de Physique du Globe de Paris, CNRS, Paris,France, [3]Jet Propulsion Laboratory, California Institute of Technology, Pasadena, CA, USA, [4]Now at NASA Goddard Space Flight Center, Greenbelt, MD, USA, Departamento Académico de Geología y Geofísica,[5]Universidad Nacional de San Agustín de Arequipa, Arequipa, Peru, [6]Observatorio Vulcanológico del INGEMMET (OVI), Arequipa, Peru, [7]Instituto Geofísico del Perú, Lima, Peru

Abstract We present evidence of volcano-tectonic interactions at Sabancaya volcano that we relate to episodic magma injection and high regional fluid pore pressures. We present a surface deformation time series at Sabancaya including observations from ERS-1/2, Envisat, Sentinel-1, COSMO-SkyMed, and TerraSAR-X that spans June 1992 to February 2019. These data show deep-seated inflation northwest of Sabancaya from 1992–1997 and 2013–2019, as well as creep and rupture on multiple faults. Afterslip on the Mojopampa fault following a 2013 M_W 5.9 earthquake is anomalously long lived, continuing for at least 6 years. The best fit fault plane for the afterslip is right-lateral motion on an EW striking fault at 1 km depth. We also model surface deformation from two 2017 earthquakes (M_W 4.4 and M_W 5.2) on unnamed faults, for which the best fit models are NW striking normal faults at 1–2 km depth. Our best fit model for a magmatic inflation source (13 km depth, volume change of 0.04 to 0.05 km^3 yr^{-1}) induces positive Coulomb static stress changes on these modeled fault planes. Comparing these deformation results with evidence from satellite thermal and degassing data, field observations, and seismic records, we interpret strong pre-eruptive seismicity at Sabancaya as a consequence of magmatic intrusions destabilizing tectonic faults critically stressed by regionally high fluid pressures. High fluid pressure likely also promotes fault creep driven by static stress transfer from the inflation source. We speculate that combining high pore fluid pressures with sufficiently large, offset magmatic inflation can promote strong earthquakes during volcanic unrest.

Key Points:
- InSAR analysis provides evidence for laterally and vertically complex volcanic plumbing system at Sabancaya
- High fluid pressure at Sabancaya promotes strong seismicity during 2012–2019 eruptive period
- High fluid pressure and static stress transfer from deep inflation promote long-lived fault creep

Supporting Information:
- Supporting Information S1

Correspondence to:
P. MacQueen,
pgm65@cornell.edu

Citation:
MacQueen, P., Delgado, F., Reath, K., Pritchard, M. E., Bagnardi, M., Milillo, P., et al. (2020). Volcano-tectonic interactions at Sabancaya volcano, Peru: Eruptions, magmatic inflation, moderate earthquakes, and fault creep. *Journal of Geophysical Research: Solid Earth*, *125*, e2019JB019281. https://doi.org/10.1029/2019JB019281

Received 20 DEC 2019
Accepted 13 APR 2020
Accepted article online 20 APR 2020

©2020. American Geophysical Union. All Rights Reserved.

1. Introduction

Volcano-tectonic (VT) seismicity often occurs with volcanic eruption and unrest (e.g., Ebmeier et al., 2016) and frequently reveals significant volcano-tectonic interactions. Large ($M_W > 4$) tectonic earthquakes can promote eruption via static stress changes (e.g., King et al., 1994) over smaller distances (e.g., <5 km at Cerro Negro, Nicaragua, La Femina et al., 2004) or via dynamic stress changes over larger distances (e.g., >50 km at Merapi, Indonesia, Walter et al., 2007). Conversely, intrusions can trigger strong seismicity, as inferred from InSAR (Interferometric Synthetic Aperture Radar) at Peulik and Akutan in Alaska (Lu & Dzurisin, 2014) and static stress calculations at Iwatesan Volcano in Japan (Nishimura et al., 2001). Two-way interactions are also possible. Static stress changes from volcanic inflation promoted large earthquakes at Chiles-Cerro Negro Volcanoes (Ecuador-Colombian border, Ebmeier et al., 2016) and Karymsky Volcano Group (Russia, Walter, 2007). At Chiles-Cerro Negro, the earthquake stress change inhibited further inflation (Ebmeier et al., 2016), while the earthquake at Karymsky instead promoted eruption (Walter, 2007).

In several volcanic crises, tectonic activity on regional faults kilometers away from the volcanic edifice preceded renewed magmatic activity (White & McCausland, 2016). White and McCausland (2016) summarize several such cases of precursory distal volcano-tectonic earthquakes ("distal VTs" or "dVTs") around the globe. These dVTs are often the earliest precursor to eruptive activity at volcanoes that have been dormant

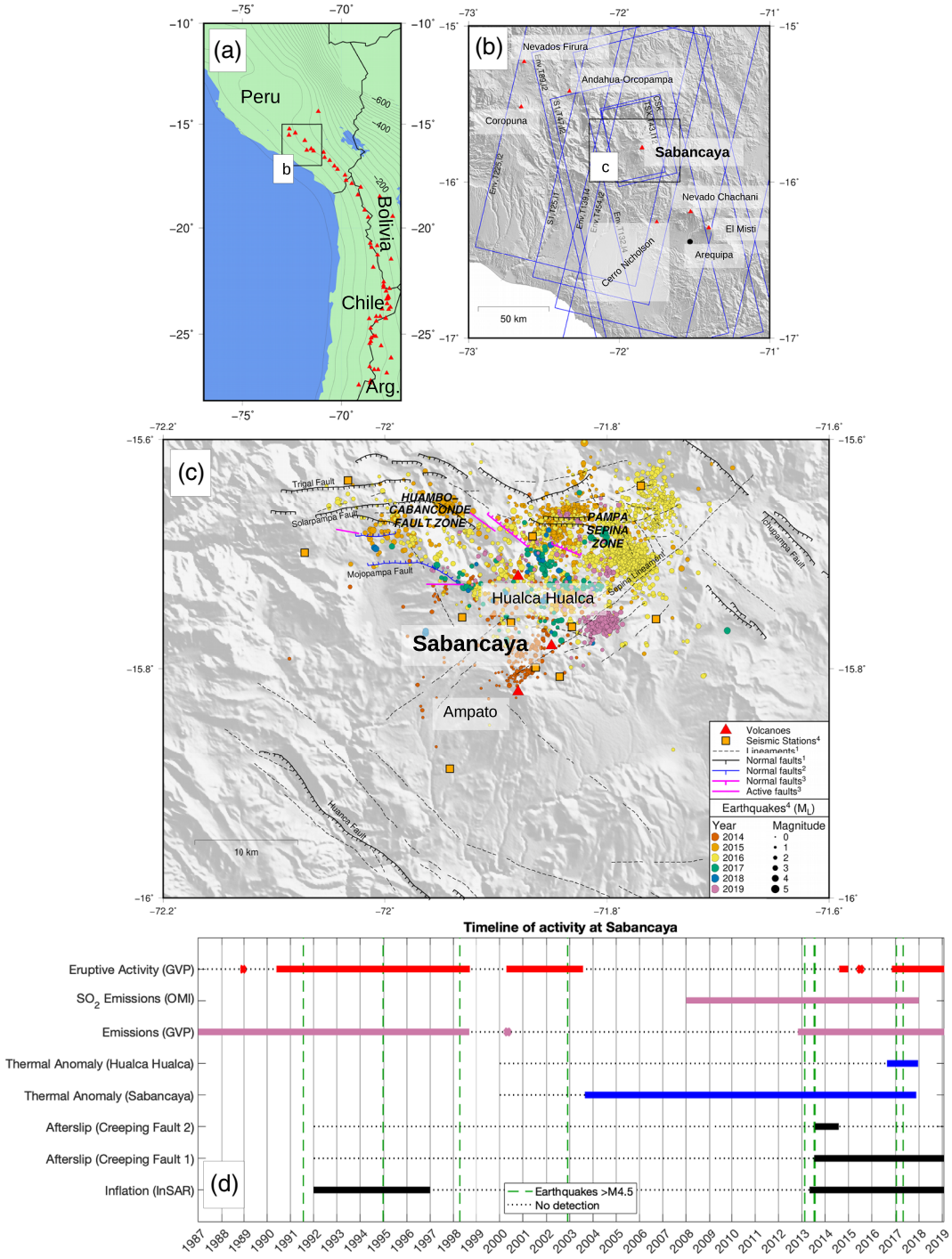

Figure 1. (a) Overview map of the Central Andean Volcanic Zone, with Holocene volcanoes (red triangles Global Volcanism Program, 2013) and subduction slab contours (gray lines Hayes et al., 2012). Black box denotes area shown in Figure 1b. (b) Map of southern Peru showing the location of Sabancaya. Blue rectangles indicate satellite tracks used in this study, and red triangles are Holocene volcanoes (Global Volcanism Program, 2013). Black circle marks the location of Arequipa. Black box denotes area shown in Figure 1c. (c) Zoom-in map of the Sabancaya region. Red triangles mark locations of Sabancaya, Hualca Hualca, and Ampato. Faults and lineaments are from [1]Antayhua et al. (2002), [2]Jay et al. (2015), and [3]this study. Filled circles are earthquakes recorded by the [4]INGEMMET seismic network (orange squares) from 2014 to 2019. (d) Timeline of activity at Sabancaya with data from the Global Volcanism Program (2013), Reath et al. (2019a), Pritchard and Simons (2004), and this study. Black dotted lines indicate time periods when data was collected but no anomaly/activity was detected. Earthquakes >M_W 4.5 included in this figure are those studied by InSAR. See Figure S1 for times of all earthquakes >M_W 4.5 within 50 km of Sabancaya. Figure modified from Figure 1 in Jay et al. (2015).

21699356, 2020, 5, Downloaded from https://agupubs.onlinelibrary.wiley.com/doi/10.1029/2019JB019281, Wiley Online Library on [17/06/2024]. See the Terms and Conditions (https://onlinelibrary.wiley.com/terms-and-conditions) on Wiley Online Library for rules of use; OA articles are governed by the applicable Creative Commons License

21699356, 2020, 5, Downloaded from https://agupubs.onlinelibrary.wiley.com/doi/10.1029/2019JB019281, Wiley Online Library on [17/06/2024]. See the Terms and Conditions (https://onlinelibrary.wiley.com/terms-and-conditions) on Wiley Online Library for rules of use; OA articles are governed by the applicable Creative Commons License

for decades or more. They begin weeks to years before the onset of volcanic activity, can occur kilometers from the volcanic edifice, and tend to die off sharply after the beginning of volcanic activity (White & McCausland, 2016). White and McCausland (2016) propose a mechanism for dVTs in which intrusion of new magma into a volcanic system pressurizes surrounding aquifers, triggering earthquakes on preexisting tectonic faults. They argue further that static stress changes from the intrusion (e.g., King et al., 1994) are unlikely to be large enough to trigger slip on faults kilometers away.

Recent tectonic activity preceding and coincident with eruptive activity at Sabancaya volcano in southern Peru (Figure 1) displays many of the features attributed to distal VTs. The rich database of deformation and thermal (Reath et al., 2019a, 2019b) and seismic data available at Sabancaya provides an ideal data set for testing the White and McCausland (2016) interpretation and mechanism for distal VT events—a chance to test a proposed "common process at unique volcanoes" (Cashman & Biggs, 2014).

Sabancaya volcano is one of the most active volcanoes in the Central Andes (Pritchard et al., 2018), with an ongoing period of unrest that began in 2012–2013 (Jay et al., 2015). Manifestations of unrest have included increased fumarolic activity, gas emissions, swarms of volcano-tectonic (VT) earthquakes, ground deformation, and explosions (Reath et al., 2019a). Explosions began in 2014 and reached a maximum of VEI 3 (volcanic explosivity index) in November 2016 (Global Volcanism Program, 2017; Machacca Puma et al., 2018). Eruptions at Sabancaya present a hazard to the surrounding region and Peru's second largest city, Arequipa (Figure 1b), through ashfall and potential contamination of the drinking water supply (Rankin, 2012).

Several different faults surrounding the volcano have had shallow-depth (<30 km) moderate earthquakes ($M_W > 4.5$) during the recent unrest, over 20 within 50 km of Sabancaya since 2013. Few earthquakes were recorded teleseismically prior to early 2013 near Sabancaya (Jay et al., 2015). The large number of earthquakes with $M_W > 4.5$ near a volcano without coincident eruption is globally unusual (Jay et al., 2015; Zobin, 2001). Given the close proximity in time and space of the elevated seismicity and eruptive activity at Sabancaya, a link between the two seems likely, but the nature of that link is unclear. A previous InSAR study using very limited data from 2002 to 2015 found no evidence for magmatic deformation above the detection threshold (Jay et al., 2015), although InSAR detected inflation had occurred between 1992 and 1997 during a previous eruptive episode (Pritchard & Simons, 2004). Moreover, higher temporal resolution SAR data collected after 2015, covering the still ongoing eruption at Sabancaya, may help elucidate any connections between tectonic and magmatic activity.

An additional atypical feature of the tectonic activity near Sabancaya is the observation of potentially aseismic slip on multiple faults. Jay et al. (2015) observed possible creep across the Solarpampa fault, an aseismic component to an earthquake swarm in 2002, and afterslip on the Mojopampa fault (Benavente et al., 2016) after it ruptured in a M_W 5.9 earthquake on 17 July 2013. These observations of fault creep are unique in a volcanic area in that they are not obviously related to flank gravitational motion, as is the case on other volcanoes (e.g., Poland et al., 2017). For crustal faults, fault creep is typically linked to changes in lithology along the fault, changes in the state of stress on the fault, and/or elevated pore pressure on the fault (e.g., Avouac, 2015; Bürgmann, 2018). Determining what permits fault creep at Sabancaya would shed light on the state of stress in the shallow crust and what conditions favor aseismic versus seismic slip.

In this paper we investigate the following three research questions:

1. Is aseismic and seismic tectonic activity at Sabancaya related to magmatic activity, and if so, how?
2. By determining the driving tectonic forces at Sabancaya, can we identify the state of tectonic faults in the region?
3. What can ground and spaced-based observations of unrest tell us about the dynamics of the magmatic system at Sabancaya?

To answer these questions, we construct interferograms and InSAR times series at Sabancaya using data from several SAR satellites. We then use these deformation data to model deformation sources, and the static stress changes from these deformation sources, focusing on InSAR detected inflation, earthquakes, and aseismic slip. We finally combine these results with other information from seismic, thermal, and degassing data to form a conceptual model of magma-tectonic interactions at Sabancaya in which high pore fluid pressures facilitate aseismic slip and promote elevated seismicity in response to perturbations to the local stress field.

2. Overview of Sabancaya

Sabancaya is located in the Central Andean Volcanic Zone, one of the three volcanic zones in South America caused by the subduction of the oceanic Nazca plate beneath the South American continental plate (Figure 1a). The region around the volcano is cut by several active normal faults, striking primarily E-W and NW-SE, perpendicular to the overall direction of shortening in the arc (Huaman-Rodrigo et al., 1993; Machare et al., 2003; Mering et al., 1996; Sébrier et al., 1985) (Figure 1c). Dalmayrac and Molnar (1981) theorize that this trench-parallel normal faulting is due to the collapse of the highest-elevation regions of the Andes, in which the compressive stresses causing thrust faulting in the lowlands are insufficient to support the highest-elevation mountains (e.g., Flesch et al., 2000; Rey et al., 2001; Selverstone, 2005).

Recent eruptive activity has included two eruptive episodes (maximum VEI 3) from 1990 to 1998 and from 2012 to the time of this writing, with additional minor eruptive activity (maximum VEI 2) in the early 2000s (Figure 1d) (Global Volcanism Program, 2013). Eruptive products range in composition from andesite to dacite (Gerbe & Thouret, 2004; Samaniego et al., 2016), and long periods of repose (decades to centuries) are common (Global Volcanism Program, 2013; Samaniego et al., 2016).

Increases in fumarolic activity heralded the reawakening of Sabancaya prior to its eruptions in the 1990s, after almost 200 years of dormancy (Figure 1d) (Antayhua et al., 2001, 2002; Gerbe & Thouret, 2004; Global Volcanism Program, 1988, 2000; Rodríguez & Uribe, 1994; Samaniego et al., 2016). Pritchard and Simons (2004) later observed uplift produced by inflation of a deep-seated source centered at Hualca Hualca (NE of Sabancaya) from 1992 to 1997(Figure 1d). Gerbe and Thouret (2004) analyzed the products of the 1990–1998 eruptive sequence and determined that a combination of magma mixing (andesite) and fractional crystallization (dacite) best explained the range from andesite to dacite in eruptive products. From 1998 to 2011 activity at Sabancaya consisted mainly of gas emissions with rare trace amounts of ash (Global Volcanism Program, 2003, 2000).

Beginning in 2003, ASTER satellite measurements detected volcanic thermal anomalies at Sabancaya (Figure 1d). Starting in 2011 these anomalies steadily increased first in temperature and then in area (Figure S2; Reath et al., 2019b). During this time the plume consisted primarily of magmatic gases with only trace amounts of ash (Figure S4; Global Volcanism Program, 2016; Machacca Puma et al., 2018). The area experienced elevated levels of seismicity, culminating in a M_W 5.9 earthquake west of Hualca Hualca on the Mojopampa fault (Figure 1c on 17 July 2013, and Figure S1; Jay et al., 2015; Puma et al., 2016). Jay et al. (2015) analyzed a limited SAR data set and seismic records for a series of earthquakes that preceded the 2014 eruption but did not detect any magmatic deformation with the available data and analysis methods used (Jay et al., 2015 did not calculate any deformation time series). Two phreatic explosions occurred in August 2014 (Global Volcanism Program, 2016; Jay et al., 2015; Puma et al., 2016).

In November of 2016 eruptive activity increased dramatically in intensity, changing from a diffuse plume of mainly magmatic gases to an ash-rich plume with several explosions per day (Figure S4; Global Volcanism Program, 2017; Manrique Llerena et al., 2018). Kern et al. (2017) measured extremely high emission rates of water vapor at Sabancaya in the 6 months prior to November 2016, consistent with the boiling off of the hydrothermal system. On 6 November 2016, vulcanian style explosions began (Instituto Geofísico del Perú, 2017). After the onset of the November 2016 eruption, the thermal output at Sabancaya was high enough to saturate ASTER thermal measurements on the next two clear acquisitions (3 and 28 April 2017) (Figure S2; Reath et al., 2019a). In late 2016 a thermal anomaly at Hualca Hualca first became visible in ASTER satellite images, significantly increasing first in temperature and then area, similar to the thermal features on Sabancaya (Figure S2). Around this time, there were reports of an increase in the activity of preexisting hydrothermal features in the area, and field observations found areas of hydrothermal activity colocated with the ASTER thermal anomalies (Macedo, 2018).

3. Data and Data Processing

In this study we use all available synthetic aperture radar (SAR) data from the Sentinel 1 A/B (S1), TerraSAR-X (TSX), and COSMO-SkyMed (CSK) SAR satellite missions spanning 2013 to 2019 as well as limited Envisat and ERS-1/2 data from 1992 to 2010 (Figure 1b and Table S1).

21699356, 2020, 5, Downloaded from https://agupubs.onlinelibrary.wiley.com/doi/10.1029/2019JB019281, Wiley Online Library on [17/06/2024]. See the Terms and Conditions (https://onlinelibrary.wiley.com/terms-and-conditions) on Wiley Online Library for rules of use; OA articles are governed by the applicable Creative Commons License

3.1. ERS-1/2 and Envisat

Only a few interferograms are available from ERS-1/2 and Envisat C-band (5.6 cm wavelength) satellites, and most have long temporal and/or perpendicular baselines (Table S1). Thus, the time series for these data sets are noisier than for the more recent data. Both data sets were processed using the ROI_PAC software package (Rosen et al., 2004)—the Envisat data by Jay (2014) and ERS-1/2 by Pritchard and Simons (2004).

To calculate a time series with the ERS-1/2 data, we used the deformation source calculated for each interferogram in Pritchard and Simons (2004) to forward model the predicted deformation at Sabancaya. We used the time series approach of Henderson and Pritchard (2013) to calculate a time series using the Envisat data.

3.2. COSMO-SkyMed

We used SAR data from the Italian Space Agency (ASI) COSMO-SkyMed (CSK) X-band (3.1 cm wavelength) four-satellite constellation. Data are from the ascending pass of the satellite. CSK data were processed using the InSAR Scientific Computing Environment (ISCE) package developed at the Jet Propulsion Laboratory (JPL), Caltech, and Stanford University (Rosen et al., 2015). ISCE processing used the Shuttle Radar Topography Mission (SRTM) 30 m digital elevation model (DEM) (Farr et al., 2007) to correct for topography. Final geocoded interferograms have a spatial resolution of 30 m. For interferogram unwrapping we used the SNAPHU unwrapper (Chen & Zebker, 2001) implemented in ISCE.

Perpendicular baselines for the CSK data were generally constrained to be within 400 min orbital separation and 3 months in temporal separation. For each acquisition, we then selected the four shortest (in time) pairs (e.g., 1-2, 1-3, 1-4, 1-5; 2-3, 2-4, 2-5, 2-6...), from the set of pairs matching the requirements mentioned above.

We computed InSAR time series from such sets of 348 interconnected interferograms using the GIAnT software package (Agram et al., 2012) in the NSBAS mode. Atmospheric corrections were not applied, as the smaller spatial footprint makes estimation of atmospheric effects harder, and the signals of interest were large enough that such corrections were not needed.

3.3. TerraSAR-X

We calculated interferograms for the TSX time series (originally calculated for Reath et al., 2019a) with perpendicular baselines less than 100 m and temporal baselines less than 1 year using the ROI_PAC software package (Rosen et al., 2004). We then down-looked interferograms by eight looks with a power spectrum filter strength between 0.2 and 0.5 (Goldstein et al., 1988), unwrapped them with the SNAPHU algorithm (Chen & Zebker, 2001), and coregistered them using the "ampcor" routine in ROI_PAC (Rosen et al., 2004). Interferograms were processed with the SRTM DEM for a final geocoded resolution of 30 m.

We calculated the TSX time series with a MATLAB implementation of the Small Baseline Subset (SBAS) time series method of Berardino et al. (2002), with no digital elevation model (DEM) error correction, which has been used in many other publications (Delgado et al., 2017; Finnegan et al., 2008; Henderson & Pritchard, 2013, 2017). DEM error corrections were not attempted because the pairs have a small temporal baseline and the satellite baseline does not drift during the acquisition time. In order to avoid removing signals of interest, no atmospheric corrections were applied, nor ramps removed, because of the small area of the TSX swath relative to the signals of interest. We instead referenced every interferogram to a stable area south of the deforming area. We found that this approach of removing a spatially constant offset did not change the results significantly with respect to removing ramps in the small nondeforming areas at Sabancaya.

3.4. Sentinel 1

We used the ISCE software package (Rosen et al., 2015) to process interferograms for the S1 data set, using the SRTM 30 m digital elevation model (Farr et al., 2007) to correct for topography. We chose interferograms to process for the S1 time series via a "daisy chain" method in which for each SAR scene we created interferograms with the next three SAR scenes chronologically. We did not use a single master SLC to create a common simulation for the whole data set. This maintains small temporal baselines, while also ensuring that each time interval is covered by multiple interferograms in case one of the interferograms has burst alignment issues (potentially due to ionospheric perturbations; e.g., Wang et al., 2017) or unresolvable unwrapping errors. We downlooked the S1 interferograms using two looks in azimuth and eight looks in range for a resolution of approximately 44 min azimuth and 25 min range prior to geocoding. After geocoding with the 30 m SRTM DEM, the resolution was 30 m. These interferograms were first unwrapped using the GRASS algorithm (Goldstein et al., 1988), and if unwrapping errors were found we redid the unwrapping

21699356, 2020, 5, Downloaded from https://agupubs.onlinelibrary.wiley.com/doi/10.1029/2019JB019281, Wiley Online Library on [17/06/2024]. See the Terms and Conditions (https://onlinelibrary.wiley.com/terms-and-conditions) on Wiley Online Library for rules of use; OA articles are governed by the applicable Creative Commons License

using the SNAPHU algorithm (Chen & Zebker, 2001). After the second pass of unwrapping, interferograms that still had unwrapping errors or burst alignment errors (e.g., Wang et al., 2017) were excluded from later time series calculations.

We calculated deformation time series from the S1 interferograms with the SBAS method (Berardino et al., 2002) using the open source software package GiANT (Agram et al., 2012). As the spatial footprint of the S1 radar images is much larger than the signals of interest, we were able to use the methods of Lin et al. (2010) to apply an empirical correction for topography-related stratified atmosphere effects to the S1 time series. This correction reduced the temporal variance of pixels in areas of high relief, particularly near the canyon north of Hualca Hualca.

We processed selected S1 interferograms for earthquake modeling with less down-looking to create higher-resolution interferograms, using one look in azimuth and four looks in range for a resolution of approximately 22 min azimuth and 12 min range for the entire interferogram prior to geocoding. After geocoding with the 30 m SRTM DEM, the resolution was 30 m. To conserve data storage space and improve processing time, we only processed these select interferograms at the higher resolution rather than the entire time series. These interferograms were unwrapped using the SNAPHU algorithm (Chen & Zebker, 2001). We masked regions of low coherence and unwrapping errors prior to modeling.

4. Modeling Strategy

In this paper we infer deformation sources for InSAR-measured deformation from two 2017 earthquakes, inflation, and a creeping fault using analytical deformation source models. These analytical models are a vast simplification of complex geology, assuming a semi-infinite, elastic, isotropic, homogeneous half space (Barnhart & Lohman, 2010; McTigue, 1987; Mogi, 1958; Newman et al., 2006; Okada, 1985; Yang et al., 1988). However, they are still useful for getting a first-order picture of the different sources of deformation at Sabancaya that will allow us to investigate any interactions between these deformation sources over the time periods of months to years.

We used S1 interferograms to model the 2017 earthquakes and deformation rate maps calculated from the TSX and S1 time series to model the roughly linear periods of inflation and long-lived fault creep. The interferograms span the events as close in time as possible, with as high a coherence as possible. We did not remove a model of the inflation from these interferograms prior to performing modeling. Relative to the scale of the earthquake deformation signals, the inflation signal is broad enough that it acts as an offset plus a ramp. As a standard step in all inversions, we fit and remove an offset and ramp from the deformation data.

Prior to inverting for source parameters, we downsampled the deformation data using the methods outlined in Lohman and Simons (2005). We found best fit deformation source parameters using the Neighborhood Algorithm (Sambridge, 1999), using the data and deformation sources described in Table S2.

We use a Young's modulus of 28 GPa for this analysis. While Hickey et al. (2013) suggests a value around 80 GPa would be appropriate for igneous rocks based on values from Gudmundsson (2011), work by Heap et al. (2019) suggests that such values may be too high, particularly when scaled up to large, fractured rock masses, and suggests a value of 5.4 GPa for volcanic areas. However, the analysis in Heap et al. (2019) applies only to shallow depths (<2 km). Therefore, we chose 28 GPa for our analysis, as an intermediate value that attempts to reflect igneous rocks in a heavily faulted area with active volcanism.

We modeled the time series for aseismic movement on the Mojopampa fault (Figure 1c) using the analytical expression of Perfettini and Avouac (2004):

$$\delta(t) = \delta_i + \frac{aH\sigma}{G} log[1 + d\frac{V_i}{V_0}(e^{(t/t_r)} - 1)] \quad (1)$$

Equation (1) calculates afterslip on a fault as a result of postseismic rate-strengthening creep in response to a dynamic or static stress perturbation. In this expression, δ_i is the initial slip, a is a unitless rate-dependent frictional parameter, H is the characteristic length of the rate-strengthening area, σ is the effective normal stress, G is the shear modulus, and t_r is the characteristic time of the afterslip. V_i and V_0 are the initial creep velocity and interseismic plate velocity, respectively. d is a unitless parameter that characterizes the change in sliding velocity in response to a coseismic shear stress change.

21699356, 2020, 5, Downloaded from https://agupubs.onlinelibrary.wiley.com/doi/10.1029/2019JB019281, Wiley Online Library on [17/06/2024]. See the Terms and Conditions (https://onlinelibrary.wiley.com/terms-and-conditions) on Wiley Online Library for rules of use; OA articles are governed by the applicable Creative Commons License

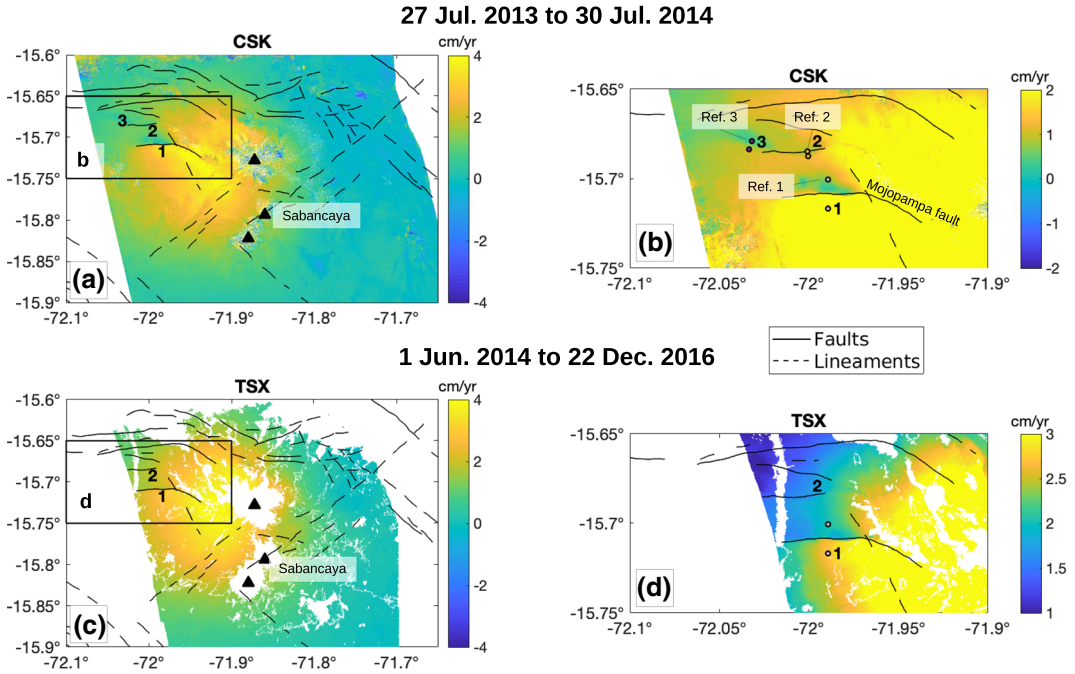

Figure 2. Maps of rate of ground displacement in satellite line-of-sight at Sabancaya showing deformation from fault creep and the beginnings of inflation at Hualca Hualca. (a and b) Displacement rates calculated from a linear time series from CSK data spanning 27 July 2013 to 30 July 2014. (c and d) Displacement rates calculated from a linear time series from TSX data spanning 1 June 2014 to 22 December 2016. Note that color scales are different between (a) and (b) and between (b) and (d) to better show fault creep in (c) and (d). Although the CSK and TSX time series both span the 17 July 2013 M_W 5.9 earthquake (modeled by Jay et al., 2015), these figures intentionally span the time period after the earthquake, the better to show smaller-scale deformation from fault creep and uplift. Numbers and colored dots indicate locations of time series points shown in Figure 8, with reference points labeled. Volcanoes are marked with black triangles. Faults and lineaments are from Jay et al. (2015) and Antayhua et al. (2002).

We solved for δ_i, t_r, and the parameter combinations $\frac{aH\sigma}{G}$ and $d\frac{V_i}{V_0}$ using the Neighborhood Algorithm (Sambridge, 1999) to find the best fit to the measured line-of-sight displacement across the Mojopampa fault.

Multiple studies (e.g., Ebmeier et al., 2016; Nishimura et al., 2001; Walter et al., 2007) have calculated changes in Coulomb static stress to investigate interactions between magmatic and tectonic deformation. Changes in Coulomb static stress from an earthquake or other pressure source can bring a fault closer to failure (King et al., 1994; Stein, 1999). Equation (2) calculates the change in Coulomb static stress ($\Delta\sigma_C$) on a "receiver" of a given geometry and type (e.g., earthquake or point source inflation) due to deformation from a "source" of a given geometry and type (King et al., 1994), where $\Delta\tau$ is change in shear stress, μ' is the effective coefficient of friction, and $\Delta\sigma_N$ is change in normal stress.

$$\Delta\sigma_C = \Delta\tau - \mu'\Delta\sigma_N \tag{2}$$

To calculate Coulomb static stress changes from the volcanic inflation and earthquakes, we used the Coulomb3.4 Matlab package by S. Toda (https://earthquake.usgs.gov/research/software/coulomb/) that uses the methods developed in King et al. (1994). We used the best fit spherical source model as the Coulomb static stress source and receiver for magmatic inflation. InSAR modeled fault planes from this study served as both sources and receivers in our calculations. We assume a value of 0.4 for μ' in line with similar studies in volcanic areas (e.g., Ebmeier et al., 2018) and a Young's modulus of 28 GPa, consistent with the deformation source modeling.

5. Results

Figures 2 and 3 show rates of InSAR detected deformation at Sabancaya from 2013–2019. A broad zone of uplift is evident in the CSK, TSX, and S1 time series (Figures 2 and 3), centered northwest of Sabancaya near

21699356, 2020, 5, Downloaded from https://agupubs.onlinelibrary.wiley.com/doi/10.1029/2019JB019281, Wiley Online Library on [17/06/2024]. See the Terms and Conditions (https://onlinelibrary.wiley.com/terms-and-conditions) on Wiley Online Library for rules of use; OA articles are governed by the applicable Creative Commons License

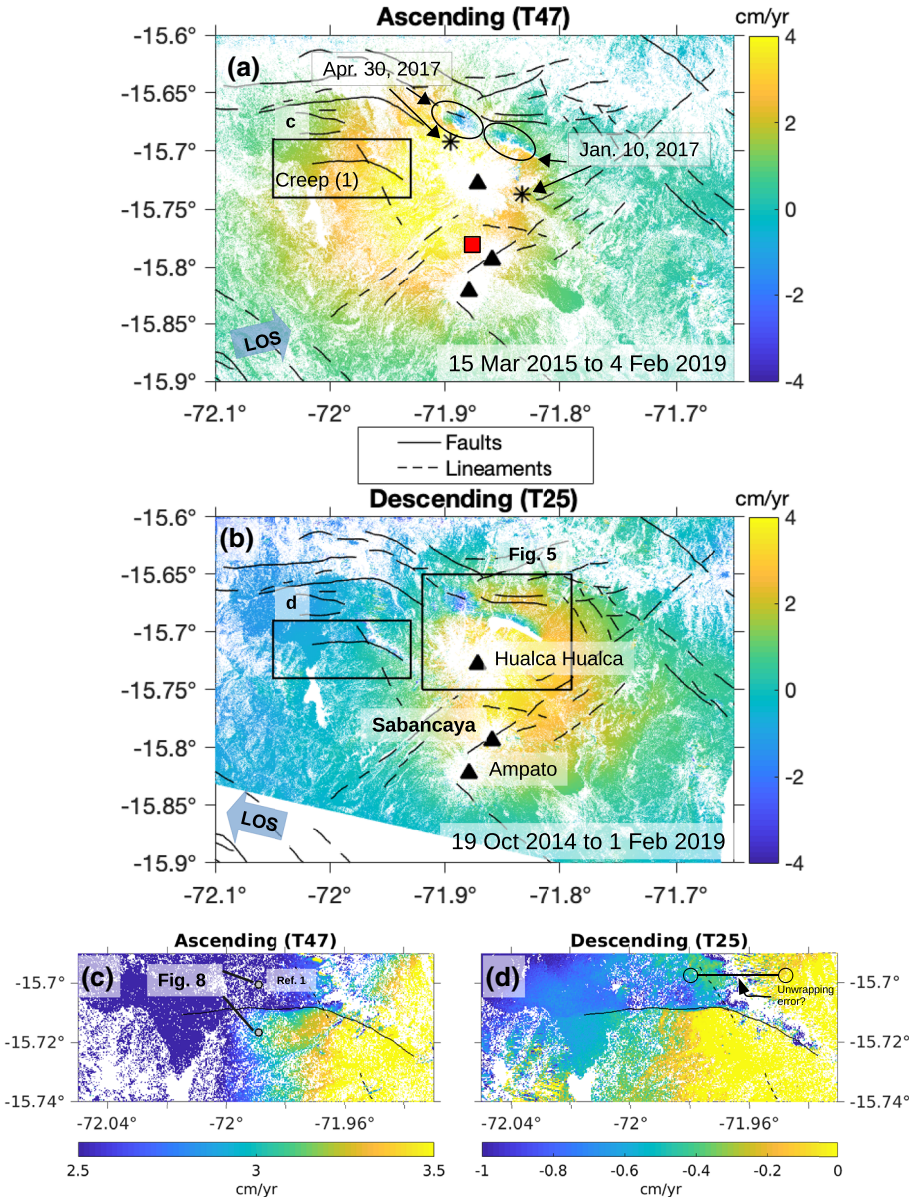

Figure 3. Maps of rate of line-of-sight deformation at Sabancaya showing deformation from inflation, fault creep (black rectangle in (a)), and two earthquake events (black ellipses, InSAR locations, and stars, epicenters from local seismic network in (a)) for the ascending (a) and descending (b) S1 tracks. Deformation rates are calculated from a linear time series from S1 data spanning 15 March 2015 to 4 February 2019 and 19 October 2014 to 1 February 2019 for the ascending and descending tracks, respectively. Volcanoes are marked with black triangles. Faults and lineaments are from Jay et al. (2015) and Antayhua et al. (2002). Black rectangle in (a) indicates area depicted in (c) and (d), and red square is the location of the time series in Figure 11a. Black rectangle in (b) indicates area depicted in Figure 5. (c and d) A zoom-in on the Mojopampa fault/Creeping Fault 1 (Figure 2). Gray dots in (c) show the points subtracted in Figure 8 to show the evolution of aseismic slip with time, with reference point noted. Note that color scales are different between (a) and (b) and between (c) and (d) to better show fault creep in (c) and (d).

Hualca Hualca. Figure 3 also shows deformation from seismic slip on two faults north of Hualca Hualca. Figures 2b and 2d feature aseismic slip on three faults west of Hualca Hualca, while Figures 3c and 3d show creep continuing on the Mojopampa fault following the 17 July 2013 earthquake through 2019 (Jay et al., 2015).

5.1. Inflation Source

The uplift rate between 2013 and 2019 creates a maximum line-of-sight displacement of approximately 3–4 cm yr^{-1} in the CSK, TSX, and S1 time series, with the point of maximum displacement located at Hualca

21699356, 2020, 5, Downloaded from https://agupubs.onlinelibrary.wiley.com/doi/10.1029/2019JB019281, Wiley Online Library on [17/06/2024]. See the Terms and Conditions (https://onlinelibrary.wiley.com/terms-and-conditions) on Wiley Online Library for rules of use; OA articles are governed by the applicable Creative Commons License

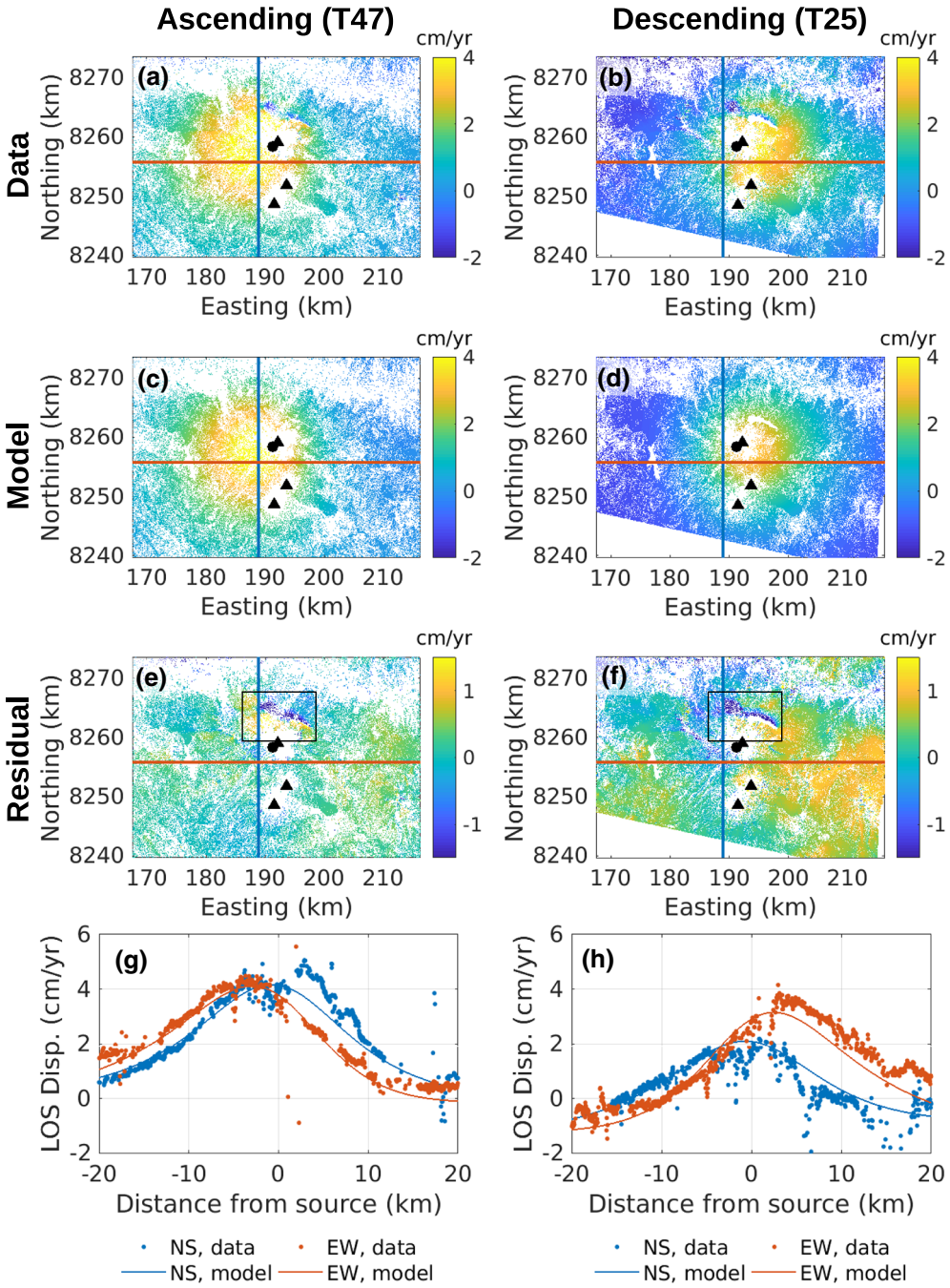

Figure 4. Spherical source modeling results for inflation source, using rate maps for ascending and descending S-1 a/b data spanning 2014–2019 (Figure 3). (a, b) Original data (full resolution), (c, d) forward modeled data, and (e, f) the residual between the data and modeled data. (g, h) NS (orange) and EW profiles (blue) of data (dots) and forward modeled data (lines). Profiles are plotted as colored lines in (a) to (f). The deformation signals from the 2017 earthquakes (black rectangles in (e) and (f)) were not removed prior to inversion, as tests showed that inversions removing the earthquake deformation model (Figure 5) produced no significant difference in the spherical source parameters.

21699356, 2020, 5, Downloaded from https://agupubs.onlinelibrary.wiley.com/doi/10.1029/2019JB019281, Wiley Online Library on [17/06/2024]. See the Terms and Conditions (https://onlinelibrary.wiley.com/terms-and-conditions) on Wiley Online Library for rules of use; OA articles are governed by the applicable Creative Commons License

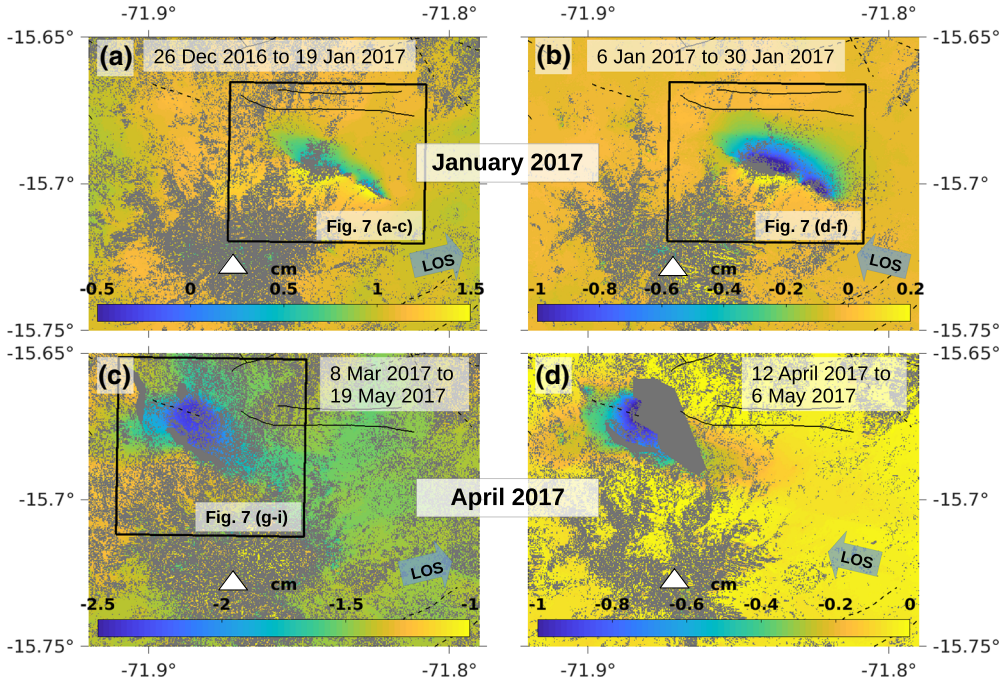

Figure 5. Unwrapped S1 interferograms spanning two small earthquakes—10 January 2017 M_W 5.0 (a, b) and 30 April 2017 M_W 5.2 (c, d). A model of the inflation signal was not removed from these data (see section 4). Unwrapping errors close to the fault (a, b, c, d) and also north of the fault (d) are masked (dark gray). The left column is data from the ascending track (T47), and the right column is from the descending track (T25). Hualca Hualca is marked with a white triangle. Faults and lineaments are from Jay et al. (2015) and Antayhua et al. (2002).

Hualca (Figures 2 and 3). The spatial footprint of the deformation signal is similar to that in Pritchard and Simons (2004) during the 1992–1997 time period.

Using a spherical source (McTigue, 1987; Mogi, 1958), the best fit model for the S1 time series (ascending and descending tracks) places the inflation at a depth of 13 km with a volume change of about 0.04 $km^3\ yr^{-1}$ (Figure 4), located within 3 km of the deformation source calculated for the 1992–1996 inflation (Pritchard & Simons, 2004). The suite of acceptable models generated by the neighborhood algorithm (Sambridge, 1999), defined as having misfit within 5% of the best fit model, yields depths ranging from 12 to 15 km, and volume changes ranging from 0.03 to 0.05 $km^3\ yr^{-1}$. We achieved similar results using a spherical source to model the TSX data (ascending track only), with a depth of 14 km and a volume change of 0.05 $km^3\ yr^{-1}$. Using both the S1 and TSX time series, the center of the inflation is centered at the inactive volcano Hualca Hualca, approximately 7 km NNW of Sabancaya. Inversion results for the inflation source with and without models of the 2017 earthquakes removed are not significantly different, so we did not remove the earthquake signals in the final inversion. These results for the depth and location of the source are consistent with modeling results for a spherical source using GPS data from 2014–2015 that find a source depth of 13 km (Taipe Maquerhua et al., 2016).

Modeling the uplift with a prolate ellipsoidal source does not significantly improve the model fit to data (Figure S5). The best fit prolate ellipsoidal source (Newman et al., 2006; Yang et al., 1988) has a depth of 13 km, a semimajor axis of 8 km, a semiminor axis of 6 km, and a pressure change of 1.2 MPa yr^{-1}. An *F* test between the two inversions gives a 98% chance of no significant difference between the two modeling scenarios, so we continue our analysis using the spherical source. The best fit ellipsoidal source also has an aspect ratio of 0.7, approaching that of a sphere, strengthening the argument for using the simpler spherical source.

5.2. 2017 Earthquakes

Multiple S1 interferograms spanning 10 January 2017 show a northwest-southeast trending region of subsidence and uplift to the northeast of Hualca Hualca (Figures 5a and 5b). The seismic catalog from the local

21699356, 2020, 5, Downloaded from https://agupubs.onlinelibrary.wiley.com/doi/10.1029/2019JB019281, Wiley Online Library on [17/06/2024]. See the Terms and Conditions (https://onlinelibrary.wiley.com/terms-and-conditions) on Wiley Online Library for rules of use; OA articles are governed by the applicable Creative Commons License

Date		InSAR	Local	NEIC	GCMT
10 January 2017	Depth (km)	1	12	3.9	-
	M_w	5.0	4.4	4.5	-
	Focal Mechanism	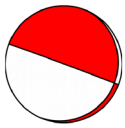	-		-
30 April 2017	Depth (km)	1.5	6.1, 8.7, 13, 13.6, 12.1	10, 10, 10	12, 21.7
	M_w	5.2	5.2, 4.1, 4.0, 4.0, 4.5	5.1, 4.6, 4.4	5.0, 4.9
	Focal Mechanism	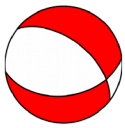	-	-,-	,

Figure 6. Comparison of depths, magnitudes, and fault source parameters for earthquakes modeled in this study, calculated from InSAR, the IGP local seismic network, the Global Centroid Moment Tensor (GCMT) catalog, and the National Earthquake Information Center (NEIC). Dashes (-) indicate no data.

seismic network records one M_L 4.4 earthquake on this date (black star in Figure 3a). To model this event, we used two unwrapped interferograms from the ascending and descending tracks (Table S3).

InSAR modeling of this event (Figure 7) gives M_W 5.0 for slip on a normal fault striking northwest dipping 89° to the northeast, a slightly larger magnitude than that calculated from the local seismic network (Figure 6). The discrepancy in magnitude is small and may reflect the inherent uncertainty in both estimates of magnitude but could indicate a small portion of the deformation occurred aseismically, potentially as afterslip that is seen after other earthquakes in the region. A distributed slip inversion shows that most of the slip occurs at 1.5 km depth, with a small region of higher magnitude slip at less than 0.5 km depth (Figure 7j). This concentration of high magnitudes of slip near the surface suggests that there may have been surface rupture associated with this event. However, evidence for this is ambiguous in the interferogram, as zones of low coherence along the fault are concentrated on a ridge, potentially indicating surface disruption (such as small landslides) rather than surface rupture. We discuss the difference in depth between the InSAR results and seismic catalogs in section 6.1. The model slightly underpredicts the amount of surface deformation (Figures 7c and 7f), although the residuals are generally below the noise level of the data. Higher amplitude residuals concentrated near the fault likely point to a more complex fault geometry not captured by slip on a uniform plane.

The local seismic catalog records five events on 30 April 2017, all located to the north of Hualca Hualca, with the largest event having a local magnitude of 5.2 (black star in Figure 3a). S1 interferograms spanning this date show an area of subsidence north of Hualca Hualca (Figures 5c and 5d). To model this event, we used an unwrapped interferogram from the ascending track (Table S3). We did not use any interferograms from the descending track to model this event as all descending interferograms covering this event suffered from unresolvable unwrapping errors (masked in Figure 5d).

Modeling of this interferogram gives a M_W 5.2 for oblique slip on a northwest striking normal fault dipping 54° to the northeast, in good agreement with the local seismic network (Figure 6). A distributed slip inversion shows that most of the slip is concentrated at 1.5 km depth (Figure 7k).

The distributed slip inversion residuals show a low amplitude (4 cm) but spatially coherent area of negative residual (Figure 7). This may be deformation from slip on another smaller magnitude event on the

21699356, 2020, 5, Downloaded from https://agupubs.onlinelibrary.wiley.com/doi/10.1029/2019JB019281, Wiley Online Library on [17/06/2024]. See the Terms and Conditions (https://onlinelibrary.wiley.com/terms-and-conditions) on Wiley Online Library for rules of use; OA articles are governed by the applicable Creative Commons License

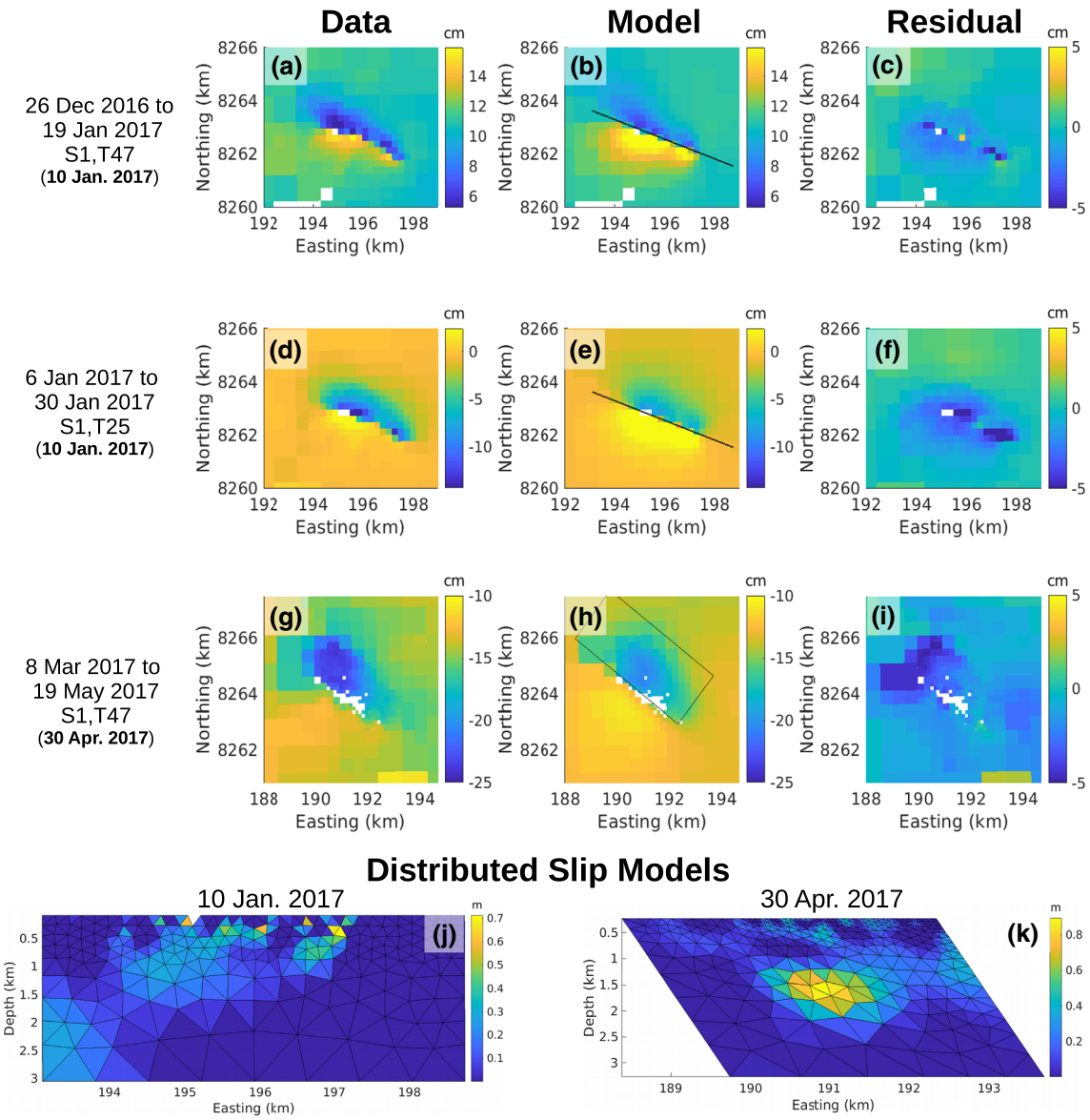

Figure 7. Modeling results for (from top to bottom) 10 January 2017 M_W 4.8 earthquake (T47 and T25) and 30 April 2017 M_W 5.2 earthquake using S1 interferograms. A model of the inflation signal was not removed from these data (see section 4). (a, d, g) The downsampled data used in inversion, (b, e, h) forward modeled data from inferred distributed slip models with the XY coordinates of the fault plane plotted (black rectangle), and (c, f, i) the residual between data and forward modeled data. (j and k) The distributed slip models for the 10 January 2017 earthquake (j) and 30 April 2017 earthquake (k).

same day. The local seismic catalog shows a M_W 4.1 event nearby at less than 10 km, providing a likely candidate for this event. It is also also possible that the April 30 M_W 5.2 earthquake is best modeled by a curved and/or more complex fault geometry.

5.3. Creeping Faults

Interferograms and time series from CSK, TSX, and S1 data reveal creep on three faults located northwest of Hualca Hualca (Figures 2 and 3). Creeping Faults 1 and 2 in Figure 2 are most likely the same faults that ruptured in the M_W 5.9 event on 17 July 2013 (Mojopampa fault) and the M_W 4.8 event on 25 July 2013, respectively, as observed by Jay et al. (2015). Using a smaller SAR data set, Jay et al. (2015) also observed aseismic slip on Creeping Fault 1 (Mojopampa fault) during the first year after the 17 July 2013 earthquake.

Figure 8a shows line-of-sight displacement across Creeping Fault 1 from March 2013 to February 2019 using CSK, TSX, and S1 data, and Figure 8b shows line-of-sight displacement across Creeping Faults 2 and 3 from July 2013 to August 2014 using CSK data. To account for differences in the line-of-sight between the different

21699356, 2020, 5, Downloaded from https://agupubs.onlinelibrary.wiley.com/doi/10.1029/2019JB019281, Wiley Online Library on [17/06/2024]. See the Terms and Conditions (https://onlinelibrary.wiley.com/terms-and-conditions) on Wiley Online Library for rules of use; OA articles are governed by the applicable Creative Commons License

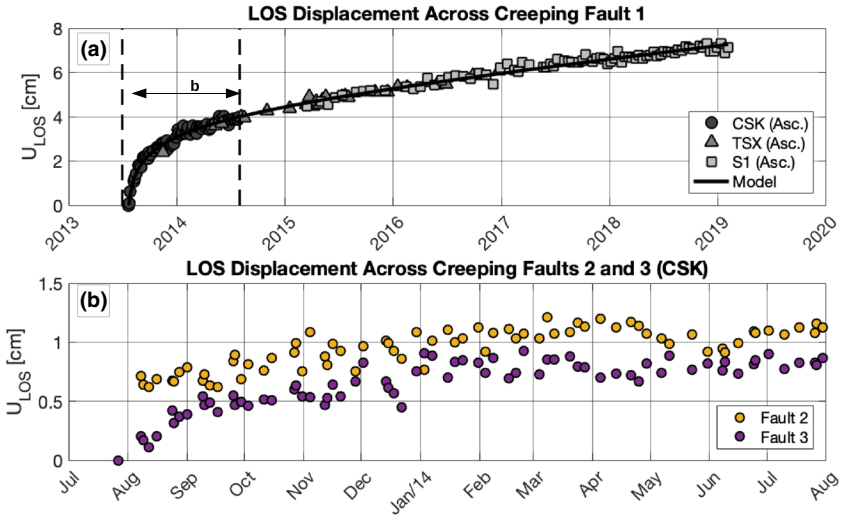

Figure 8. Line-of-sight displacements across creeping faults at Sabancaya. (a) Difference between points (gray dots in Figure 3c) spanning Creeping Fault 1/Mojopampa fault (Figure 2) from 23 July 2013 to 4 February 2019 (gray dots in Figure 3c). Circles are from the CSK time series (23 July 2013 to 30 July 2014), triangles are from the TSX time series (15 November 2013 to 22 December 2016), and squares are from the S1 time series (ascending, track 47, 15 March 2015 to 4 February 2019). Displacement is displayed relative to displacement in CSK time series on 23 July 2013. Black line is the best fitting analytical function for frictional afterslip (Perfettini & Avouac, 2004). (b) Displacement across Creeping Faults 2 and 3 (Figure 2) from 23 July 2013 to 30 July 2014, using CSK time series data. Note that these figures span a slightly different time period than Figure 2 to better show the onset of aseismic slip.

satellites in Figure 8a, we empirically corrected the slope of the TSX data by 2 cm yr^{-1} to match the slope of the temporally overlapping S1 data. In the first 6 months after the 17 July 2013 M_W 5.9 event, afterslip on Creeping Fault 1/Mojopampa fault was relatively rapid at a rate of 2–8 cm yr^{-1}. After about 1 year, the afterslip decayed to a constant rate of 0.5–0.6 cm yr^{-1} that continues to February 2019 (Figure 8a). Using Equation (1), we find a characteristic time t_r of 1.5 years best fits the data (black line in Figure 8a). For Creeping Faults 2 and 3, afterslip is much smaller magnitude (<2 cm in line-of-sight), and decayed to zero displacement after about 5 months.

Using a deformation rate map calculated from the TSX time series spanning November 2013 to December 2016 (ascending track only), the best fit model for slip on Creeping Fault 1 (Mojopampa fault) is right-lateral motion at a depth of 1 km of an east-west striking fault dipping 78° to the north, with a yearly moment release of M_w 4.4 (Figure 9). The location of the modeled slip is consistent with slip on the Mojopampa fault, at a shallower depth than the slip of the 2013 earthquake modeled in Jay et al. (2015). The small amplitude of the surface deformation precluded distributed slip modeling. We did not attempt to model any aseismic slip on the eastern branch of the Mojopampa fault, as our InSAR data does not have resolution in that area of steep relief.

5.4. Seismic and Aseismic Active Faults at Sabancaya, 1992–2019

Figure 10 shows a map of faults near Sabancaya with InSAR detected slip between 1992 and 2019 (this study; Jay et al., 2015; Pritchard & Simons, 2004), along with ASTER satellite detected thermal anomalies (this study; Reath et al., 2019a) and hydrothermal features mapped in the field (Macedo, 2018). Faults where the sense of slip is shown via black hash marks have either been previously mapped in the field or modeled from InSAR data (this study; Jay et al., 2015). See Figures S6 and S7 in the supporting information for ERS and TSX interferograms that show fault slip in 1998 and 2013.

InSAR detected slip is most frequently observed on the west, northwest, and north sides of Hualca Hualca (Figure 10). Interferograms that span large earthquakes in 1998 and 2013 show slip on multiple faults to the west of Hualca Hualca in both 1998 and 2013 (Figures S6 and S7). The hydrothermal activity at Hualca Hualca occurred directly on faults that ruptured in 2017 (Figure 10).

21699356, 2020, 5, Downloaded from https://agupubs.onlinelibrary.wiley.com/doi/10.1029/2019JB019281, Wiley Online Library on [17/06/2024]. See the Terms and Conditions (https://onlinelibrary.wiley.com/terms-and-conditions) on Wiley Online Library for rules of use; OA articles are governed by the applicable Creative Commons License

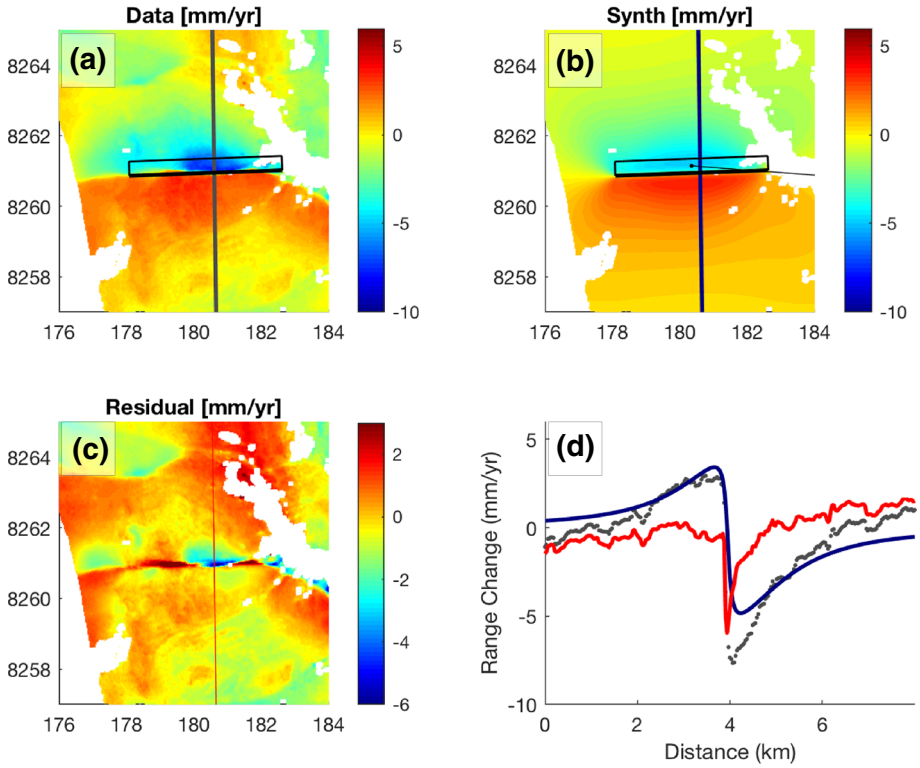

Figure 9. Modeling results for Creeping Fault 1 (Mojopampa Fault), using a surface deformation rate map calculated from the TSX time series (ascending) spanning November 2013 to December 2016. (a) Full resolution data used for inversion. (b) Predicted deformation from best fit model geometry and slip. Modeled fault indicated with black box. (c) Residual between data and predicted deformation. (d) Profiles of range change for north-south profiles across the fault. Gray dots are original data (gray line in a), blue line is predicted data (blue line in b), and red line is the residual red line in c). Modeled fault plane indicated with black box in (a) and (b).

5.5. Coulomb Static Stress Changes

The inflation source described above creates a positive Coulomb stress change on the faults for the two 2017 earthquakes, as well as on Creeping Fault 1/Mojopampa fault (Figure S8). Assuming a start time for the inflation of May 2013 and a constant inflation rate, the January 2017 fault experienced an approximately 0.08 MPa increase in Coulomb stress prior to slipping, and the April 2017 fault experienced an approximately 0.05 MPa increase. Although low, the increase in Coulomb static stress should be sufficient to promote slip on the January 2017 earthquake fault (Stein, 1999; Toda & Stein, 2003; Wauthier et al., 2016). However, the stress change on the April 2017 earthquake, although positive, is much less, so the evidence for static stress triggering on this fault is uncertain. Creeping Fault 1 also experienced a static stress increase of approximately 0.01 MPa yr^{-1}, a cumulative static stress change of approximately 0.04 MPa from May 2013 to February 2019. As for the 2017 earthquake faults, this magnitude of Coulomb stress change should be enough to promote slip on this fault (Toda & Stein, 2003; Stein, 1999; Wauthier et al., 2016).

We also found that the M_W 5.9 earthquake on the Mojopampa fault in 2013 did not cause a static stress change sufficient to promote slip on any of the 2017 earthquake faults. None of the earthquakes in 2017 caused a static stress change sufficient to promote slip on the Mojopampa fault. Jay et al. (2015) similarly found that static stress changes from seismogenic faults in 2013 were insufficient to trigger any of the InSAR modeled earthquakes activity in 2013.

5.6. Timeline of Activity at Sabancaya

Figure 11 shows time series of inflation and hydrothermal activity at Sabancaya from 1992 to 2019. The location of the inflation time series is marked as a red square in Figure 11b. The inflation time series includes data from ERS 1 and 2, ENVISAT, ALOS, TSX, and S1. The hydrothermal time series includes ASTER data at Sabancaya (previously published in Reath et al., 2019a) and Hualca Hualca, and OMI degassing data

21699356, 2020, 5, Downloaded from https://agupubs.onlinelibrary.wiley.com/doi/10.1029/2019JB019281, Wiley Online Library on [17/06/2024]. See the Terms and Conditions (https://onlinelibrary.wiley.com/terms-and-conditions) on Wiley Online Library for rules of use; OA articles are governed by the applicable Creative Commons License

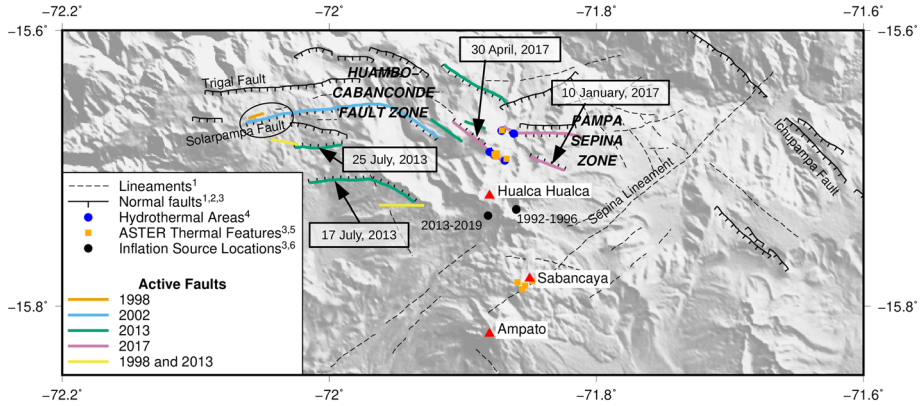

Figure 10. Active faults (seismogenic and aseismic) at Sabancaya imaged by InSAR (1998 to 2019), hydrothermal areas active from 2013 to 2019, and inflation sources active from 1992–1996 and 2013–2019 (See Figure 11). See Figures S6 and S7 in the supporting information for interferograms that show the active faults in 1998 and 2013. Faults related to a main earthquake event are labeled with the date of the earthquake. All other faults mapped as active represent likely secondary, triggered slip from a main earthquake event. Black ellipse marks section of the Solarpampa fault that slipped in 2002 (see Figure 2 of Jay et al., 2015). Faults and lineaments are from [1]Antayhua et al. (2002),[2]Jay et al. (2015), and [3]this study. Hydrothermal areas are from [4]Macedo (2018). ASTER thermal anomalies are from [3]this study and [5]Reath et al. (2019a). Inflation sources are from [3]this study and [6]Pritchard and Simons (2004).

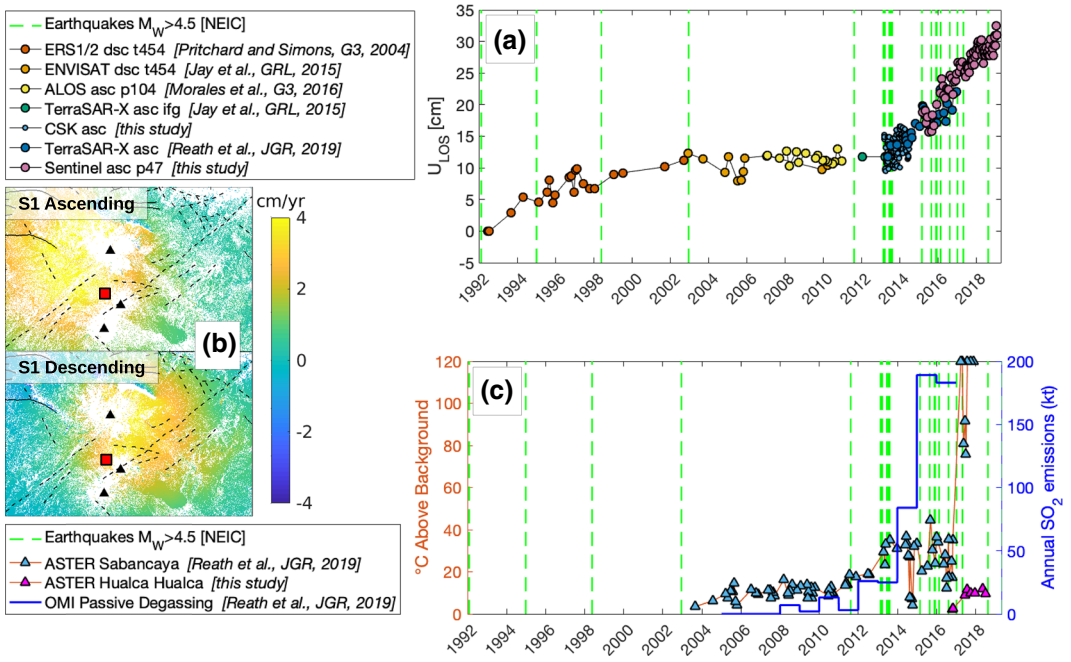

Figure 11. Detailed time series of activity at Sabancaya. Earthquakes >M_W 4.5 included in this figure are those studied by InSAR. See Figure S1 for times of all earthquakes >M_W 4.5 within 50 km of Sabancaya. (a) Line-of-sight inflation time series at Sabancaya (red square in (b) and Figure 3a) derived from ERS (Jay, 2014; Pritchard & Simons, 2004), ENVISAT (Jay, 2014; Jay et al., 2015), ALOS (Morales Rivera et al., 2016), CSK (this study), TSX (Reath et al., 2019a), and S1 (this study) data. Note that although this time series mixes ascending and descending data, the point at Sabancaya is chosen such that the amplitude of the uplift signal is as close as possible between ascending and descending. For the ALOS portion of the time series, we used the dates of the ALOS-1 images from Morales Rivera et al. (2016) and added synthetic noise with the same amplitude as the ERS and ENVISAT time series to simulate a time series with no deformation. (b) For reference, S1 maps of rate of ground displacement from Figure 3 with location of time series in (a) marked with red square. (c) Thermal anomalies at Hualca Hualca (this study) and thermal and SO_2 degassing anomalies at Sabancaya (originally published in Reath et al., 2019a).

21699356, 2020, 5, Downloaded from https://agupubs.onlinelibrary.wiley.com/doi/10.1029/2019JB019281, Wiley Online Library on [17/06/2024]. See the Terms and Conditions (https://onlinelibrary.wiley.com/terms-and-conditions) on Wiley Online Library for rules of use; OA articles are governed by the applicable Creative Commons License

21699356, 2020, 5, Downloaded from https://agupubs.onlinelibrary.wiley.com/doi/10.1029/2019JB019281, Wiley Online Library on [17/06/2024]. See the Terms and Conditions (https://onlinelibrary.wiley.com/terms-and-conditions) on Wiley Online Library for rules of use; OA articles are governed by the applicable Creative Commons License

(previously published in Carn et al., 2017; Reath et al., 2019a). The different satellites in Figure 11a have different line-of-sight (LOS) geometries, which will create discrepancies in observed amount of displacement. While we have chosen a location for the time series that minimizes the difference in displacement between ascending and descending tracks, we estimate that the different LOS between satellites could create discrepancies of up to 30%. Even given these possible discrepancies, the inflation rate in the 2013–2019 eruptive episode is significantly higher than in the previous inflation from 1992 to 1996 (Pritchard & Simons, 2004). For the current eruptive episode, inflation is first evident as of May 2013 in both the CSK and TSX time series (Figure 11a). The roughly linear trend of uplift from 2013 to 2019 agrees with GPS observations beginning in 2016 that also show a similar, steady uplift (Cruz et al., 2018; Machacca Puma et al., 2018).

6. Discussion

6.1. Discrepancies Between InSAR and Seismic Catalog Fault Depths and Locations

The InSAR depths for the earthquakes modeled in this study are significantly shallower than the depths in the global catalogs (Global Centroid Moment Tensor/CGMT, National Earthquake Information Center/NEIC), and epicenters are shifted by by several kilometers, although these discrepancies are consistent with those reported in other comparison of InSAR focal mechanisms and centroid moment tensor (CMT) catalogs, particularly given the small size ($<M_w$ 6) of the events (e.g., Devlin et al., 2012; Holtkamp et al., 2011; Weston et al., 2011). The larger depth discrepancy for the January 2017 event between InSAR results and the local seismic catalog could be partially due to the velocity model used for the local catalog or the network geometry (Mellors et al., 2004). A full waveform inversion of local or teleseismic seismic records as in Devlin et al. (2012) could potentially reduce the discrepancy between InSAR and local and global seismic catalog depths, but this is beyond the scope of this study. Mellors et al. (2004) and Gaherty et al. (2019) find no significant difference between a homogeneous and heterogeneous half-space model in their modeling of larger seismic events. We do not believe that the discrepancy can be explained as an effect of using homogeneous half-space modeling, rather than a more complex model. Visual inspection of the interferogram for the January and April 2017 earthquakes (Figure 5) also suggests that the earthquakes are indeed much shallower than the depths listed in seismic catalogs. The interferograms are incoherent along the trace of the fault (incoherence masked in Figure 5), suggesting possible surface rupture. Based on this consideration of the possible causes of discrepancies between our results and other data sources, we conclude that the InSAR depths are more accurate than those from the local or global seismic catalogs.

6.2. Modeling Limitations

The deformation source models and the Coulomb static stress modeling presented in this paper assume a semi-infinite, elastic, isotropic, homogeneous half space, a simplification with the potential to bias the results presented here. Lateral and vertical heterogeneity in elastic modulus, as well as topographic effects, can shift the location and depth of the deformation source by kilometers (e.g., Hickey et al., 2013, 2016), while viscoelastic behavior can mask relaxation as continued pressure change (e.g., Hickey et al., 2013). This implies that the offset between the inflation detected in this study and Sabancaya could be partially or entirely an effect of topography or subsurface heterogeneity. Changes to the effective elastic modulus, or a change in the location of the inflation source relative to the modeled faults, could also change the Coulomb static stress changes we calculated. While the numerical modeling necessary to resolve these issues is beyond the scope of this study, we note that the location of the inflation is consistent with areas of elevated seismicity (Figure 1c) and hydrothermal activity (Figures 10 and S3), so we are reasonably confident that the location of the inflation is not simply an artifact of modeling.

6.3. Offset Inflation at Hualca Hualca

The offset inflation observed at Sabancaya in both the 2010s and the 1990s (Pritchard & Simons, 2004), centered approximately 7 km NNW of Sabancaya, is not unique among volcanic systems. In a survey of volcanic deformation detected via satellite observations, Ebmeier et al. (2018) observes that 24% of detected deformation is centered more than 5 km from the nearest active volcanic edifice, which the authors interpret as compelling evidence for laterally extensive, complex magmatic plumbing systems (e.g., Cashman et al., 2017). The best fit spherical sources for both episodes of inflation at Sabancaya are within less than 5 km of each other, suggesting pressurization of the same zone of magma storage in both episodes. This offset inflation may illuminate activity in the deeper section of a laterally and vertically extensive complex of dikes and sills beneath Hualca Hualca, Sabancaya, and Ampato.

21699356, 2020, 5, Downloaded from https://agupubs.onlinelibrary.wiley.com/doi/10.1029/2019JB019281, Wiley Online Library on [17/06/2024]. See the Terms and Conditions (https://onlinelibrary.wiley.com/terms-and-conditions) on Wiley Online Library for rules of use; OA articles are governed by the applicable Creative Commons License

In both recent episodes of eruptive activity, the temporal behavior of the inflation does not correlate strongly with changes in eruptive behavior at the surface (Figure 1d) (Global Volcanism Program, 2000; Pritchard & Simons, 2004). Throughout the current eruptive sequence at Sabancaya, uplift continues linearly, without any changes in rate, even with the drastic change in eruptive activity in November 2016 (Figure 11a). However, the consistent observation of inflation in both of these eruptive episodes suggests some connection between the magma plumbing systems beneath Hualca Hualca and Sabancaya.

A possible interpretation of the offset inflation could be mafic recharge at depth, as proposed by Gerbe and Thouret (2004) for Sabancaya based on petrologic data and suggested at other volcanic systems by measurement of excess SO_2 (e.g., Edmonds et al., 2001, 2010). In the model proposed by Gerbe and Thouret (2004), mafic recharge at depth induces magma mixing in a preexisting dacitic magma reservoir slowly differentiating through open system crystallization. From our calculations in section 5.1, we suggest that the persistent inflation source at 13 km depth is the geophysical signature of this mafic recharge at depth.

We speculate that mafic magma then moves laterally from a temporary zone of accumulation beneath Hualca Hualca to a shallower (6 km), storage zone where magma mixing occurs between the fresh mafic magma and degassed, dacitic magma (e.g., Gerbe & Thouret, 2004), ultimately triggering eruptive activity at the surface. Temporary deflections in GPS-measured uplift at Sabancaya's summit immediately preceding increases in the number of hybrid earthquakes may be evidence for a smaller, shallow magma chamber near Sabancaya's summit (Cruz et al., 2018). Additionally, earthquake locations from 2015 to 2017 provide some evidence for possible magma transfer between Hualca Hualca and Sabancaya (Anccasi Figueroa et al., 2018).

If the offset between the inflation center and Sabancaya is an artifact of the modeling assumptions (e.g., Hickey et al., 2016), the magma transfer could be vertical magma transfer only. However, evidence for laterally connected magma plumbing systems has been found at multiple other arc volcanoes, including Karymsky (Russia) and Katmai (Alaska) (Eichelberger et al., 2000), Cerro Negro-El Hoyo Complex (Nicaragua, MacQueen et al., 2016; Venugopal et al., 2016), and Agung/Batur (Indonesia, Albino et al., 2019). This may indicate that these lateral connections are more common than previously thought.

Voluminous degassing at Sabancaya suggests that the shallow magma storage zone is more open (Kern et al., 2017; Moussallam et al., 2017; Reath et al., 2019a) (using the definition for “open” proposed by Chaussard et al., 2013), perhaps explaining why no inflation has been observed centered at Sabancaya. This could explain the partial temporal disconnect between inflation episodes and eruptive activity and fits with Reath et al.'s (2019a) classification of Sabancaya as “partially open.” While the mafic intrusion reactivates the system and potentially induces magma mixing, triggering the whole sequence of unrest, it does not directly trigger pulses of eruptive activity.

6.4. Fault Creep at Sabancaya

Aseismic movement on tectonic faults appears to be relatively common near Sabancaya, manifesting as fault creep, afterslip, and triggered slip. The InSAR time series in this study reveal aseismic fault movement on several faults northwest of Hualca Hualca (Figures 2, 3, and 8). Jay et al. (2015) report possible aseismic movement in this area in the early 2000s based on the discrepancy between the cumulative seismic moment reported in earthquake catalogs and the seismic moment calculated from InSAR-observed deformation. The authors also record creep on the Solarpampa fault in the same time period, although the magnitude of this creep is likely small.

Static stress transfer may be important for driving the long-lived aseismic slip on the Mojopampa fault (Creeping Fault 1 in Figures 8 and S8). After an initial period of afterslip, creep on this fault continues linearly, in tandem with the continuing inflation (Figures 8 and 11). Although long-lived afterslip on a normal fault is not unprecedented in this tectonic setting, the longest recorded afterslip in this region lasted for only 1 year (Xu et al., 2019), far less than the 5+ years of creep observed in this study. For the Hayward fault in California, Schmidt and Bürgmann (2008) found that, after an earthquake, creep resumed when the ratio of shear to normal stress matched the value of this ratio prior to the earthquake. We posit that a steady rate of static stress transfer from the inflation source to the Mojopampa fault may create an optimal ratio of shear to normal stress on the fault that helps drive the long-lived creep, analogous to tectonic loading on creeping sections of the San Andreas fault (Schmidt & Bürgmann, 2008). Similarly, Lundgren et al. (2017) found that inflation at Copahue volcano also promoted aseismic normal slip on faults at the volcano's summit.

21699356, 2020, 5, Downloaded from https://agupubs.onlinelibrary.wiley.com/doi/10.1029/2019JB019281, Wiley Online Library on [17/06/2024]. See the Terms and Conditions (https://onlinelibrary.wiley.com/terms-and-conditions) on Wiley Online Library for rules of use; OA articles are governed by the applicable Creative Commons License

High pore fluid pressures likely also promote creep. The injection of fluids has been observed to induce aseismic slip on faults (Bürgmann, 2018), and rate state friction modeling suggests that high pore fluid pressures should favor stable slip and extended afterslip (Segall & Rice, 1995). Although all instances of fault creep occur in an area west of Sabancaya that lacks surface evidence of hydrothermal activity, the close timing between aseismic slip on the faults west of Hualca Hualca, and reinvigorated hydrothermal activity at Sabancaya (Figure 1d, timing of aseismic slip, Figure 11d, increase in thermal anomaly temperature), is suggestive of a link.

While static stress transfer from continuing inflation, along with high pore fluid pressures, may explain the long-lived creep on the Mojopampa fault, this does not explain why this fault and others creep rather than rupture seismically. At other volcanoes, fault creep is often related to collapse of the volcanic edifice (e.g., Poland et al., 2017). However, we argue that the geometry of the creeping faults near Hualca Hualca are inconsistent with flank collapse and are too far away from the summit of Hualca Hualca to be considered part of the flanks of the volcano.

Instead, lithological differences may explain the tendency for aseismic creep in this area. Geologic maps of the area near the creeping faults show outcrops of Jurassic age sedimentary rocks, in contrast to andesitic flows in the area near the 2017 earthquakes (Benavente Escobar et al., 2018). We propose that these sedimentary rocks exhibit rate-strengthening behavior that promotes aseismic slip. This is consistent with observations of extended afterslip in thicker sedimentary basins (e.g., Lienkaemper & McFarland, 2017). More generally, multiple studies have identified lithological controls on the mode of fault slip along the length of a fault (e.g., Avouac, 2015; Bürgmann, 2018).

6.5. Connection Between Magmatic and Tectonic Activity

Possible explanations for the strong seismicity during Sabancaya's recent eruptive sequence include (1) normal tectonic activity, (2) static stress transfer from the inflation source, and/or (3) a pulse of elevated pore fluid pressure (e.g., White & McCausland, 2016). The earthquakes modeled in this study and that of Jay et al. (2015) are consistent with regional fault trends. Normal faulting is expected in this region due to a rotation of the stress tensor in areas of high relief (Dalmayrac & Molnar, 1981; Devlin et al., 2012; Mering et al., 1996; Wimpenny et al., 2018). However, the region within 50 km of Sabancaya experienced no seismic activity between 2013 and the end of eruptive activity in 2002, except for one earthquake in 2011 (Figure S1). One possible explanation for the recent uptick in seismicity in this region could be simple clustering of seismicity, in which time periods with several earthquakes are separated by long periods of quiet as part of the normal seismic cycle (e.g., Kagan & Jackson, 1991; Marco et al., 1996). However, shallow seismicity over the period of time covered by the NEIC catalog (1950 to 2019) is also spatially clustered around Sabancaya (Figure S9). The clustering of this seismicity in both time and space, close to volcanic inflation, strongly suggests that the two are linked by more than coincidence.

Our results show that static stress transfer from the inflation source was sufficient to promote the 2017 earthquakes. By 2017, the buildup of static stress from ongoing inflation is sufficient to explain the two M_W 4.5+ earthquakes modeled in this study. However, static stress transfer cannot explain the seismic activity in 2013, as the seismic activity in 2013 roughly coincides with the beginning of detectable inflation (Figure 11a), when accumulated static stress from the inflation would be insufficient to promote slip.

An alternative way to explain the earthquake activity in 2013 may be a fluid pressure pulse caused by an incipient volcanic intrusion (e.g., White & McCausland, 2016). We have evidence of an increase of both heat and fluids to the area from a satellite-observed thermal anomaly at Sabancaya that increased in temperature and size around the time of the first phreatic eruption in 2013 (Reath et al., 2019b) and 2016 measurements of anomalously high levels of water vapor in Sabancaya's plume. It may be that an increase in fluid pressure in the surrounding aquifers caused regional tectonic faults to slip early in their seismic cycle, as in the mechanism for “distal VTs” proposed by White and McCausland (2016).

Repeated triggered slip of regional tectonic faults suggests that the area around Sabancaya is at a critical state of stability (Figures 10, S6, and S7). The M_W 5+ earthquakes in both 1998 and 2013 appear to have triggered slip on several smaller surrounding faults, consistent with dynamic triggering from the larger earthquakes (Figures S6 and S7). We interpret this as evidence that the area around Sabancaya is critically stressed by high fluid pore pressures, such that any stress perturbation in the area, whether from a large earthquake or a magmatic intrusion, will lead to a flurry of triggered slip on regional tectonic faults.

Aqueous fluids may have also influenced the 2017 earthquakes in addition to static stress transfer. Both satellite (Figure 11c) and field observations (Macedo, 2018) show an increase in the area and intensity of a thermal anomaly related to fumarole fields on the north flank of Hualca Hualca (Figures 10, 11c, and S2) beginning in 2016. The trace of the April 2017 earthquake, when projected to the surface, aligns well with two of these fumarole fields (Figure 10; Macedo, 2018). Both of the 2017 earthquakes occur in this region of reinvigorated hydrothermal activity. This suggests that increased pore pressure in the faults may have triggered slip on these faults in 2017, already primed to slip by static stress transfer from the inflation at depth. Ebmeier et al. (2016) also invoke a combination of static stress change from volcanic inflation and increase in fluid pore pressure to explain a M_W 5.6 earthquake near Chiles-Cerro Negro volcanoes.

While the evidence considered in this paper supports contributions from both static stress transfer and elevated fluid pore pressures to explain the strong seismicity at Sabancaya, our ability to determine the relative contributions of each of these mechanisms is limited. If the static stress transfer is much smaller than we calculate, due to the model limitations discussed in section 6.2, the relative important of pore pressure may be greater. Mapping the subsurface hydrothermal system, for example, using electrical methods (e.g., Byrdina et al., 2013; Comeau et al., 2016), could more accurately identify areas where we would expect high pore fluid pressures. Subsurface mapping of the hydrothermal system could also clarify what determines the location of creep at Sabancaya. Further work could also include more detailed modeling of the fluid pressure pulse itself (e.g., Miller et al., 2004), in order to better constrain the timing and magnitude of the pressure perturbation needed to trigger the observed seismicity.

6.6. Comparison With Other Volcanic Systems

Multiple other volcanic systems have similar features to Sabancaya (deformation and/or extensive hydrothermal systems) but lack large earthquakes. We argue that the key factors contributing to large ($>M_W$ 4.5) earthquakes at Sabancaya are the combination of (1) the magnitude of the deformation, (2) the extensive hydrothermal activity, and (3) uplift offset 5 km from the active volcano beneath an area of low heat flow that allows larger seismogenic faults. Ubinas volcano is located in southern Peru with a similar tectonic environment (Dalmayrac & Molnar, 1981) and volume of degassing (Moussallam et al., 2017) but unlike Sabancaya does not experience significant deformation or large magnitude seismicity (Figure S9; Global Volcanism Program, 2013; Reath et al., 2019a). Similar to Sabancaya, Three Sisters Volcano in the United States experienced uplift in an area offset from the summit, in an area with likely low heat flow conducive to larger faults, but the area lacks any signs of hydrothermal activity (Riddick & Schmidt, 2011) that might point to high pore fluid pressures. Cordon Caulle (Delgado et al., 2018) and Laguna del Maule (Singer et al., 2018) in Chile, and Sierra Negra in the Galapagos, Ecuador (Chadwick et al., 2006), have all experienced meter-scale deformation. Of those three, only Sierra Negra has experienced large earthquakes in its trapdoor-faulting episodes (Chadwick et al., 2006), which involve very large faults bounding the caldera.

Iwatesan volcano in Japan has many of the features we identify as crucial at Sabancaya for promoting large earthquakes, and in 1998 a M_W 6.1 earthquake occurred on a known Quaternary fault close to the volcano (Nishimura et al., 2001). The volcano has a well-known geothermal area, and beginning months before the earthquake, InSAR satellite measurements detected uplift offset from the edifice (Nishimura et al., 2001). Nishimura et al. (2001) calculated a volume change of 0.03 km^3, comparable to what we find for Sabancaya, and found that the Coulomb static stress change from the inflation promoted slip on the fault that ruptured. The 2013–2015 unrest at Chiles-Cerro Negro volcanoes also presents a good comparison to Sabancaya. In this case, inflation offset 10–15 km from the edifice triggered a M_W 5.6 earthquake on a preexisting tectonic fault in a geothermal area south of the volcanoes (Ebmeier et al., 2016). These are positive demonstrations of how magmatic inflation, an extensive hydrothermal system but limited heat flow above the deformation source, and large existing faults can conspire to produce large earthquakes in volcanic areas.

6.7. A Conceptual Model for Magma-Tectonic Interactions During the 2012–2019 Eruption at Sabancaya

In our conceptual model for Sabancaya, a critically fluid saturated crust keeps preexisting tectonic faults close to failure. The stress perturbation from an incipient magmatic intrusion creates a fluid pressure pulse that rapidly destabilizes regional faults, leading to a dramatic uptick in seismicity. As the intrusion grows in size, static stress transfer from the inflation drives creep and pushes faults closer to failure, helped along by regionally high pore fluid pressures. Figure 12 depicts the stages of unrest at Sabancaya for the most recent episode of eruptive activity.

21699356, 2020, 5, Downloaded from https://agupubs.onlinelibrary.wiley.com/doi/10.1029/2019JB019281, Wiley Online Library on [17/06/2024]. See the Terms and Conditions (https://onlinelibrary.wiley.com/terms-and-conditions) on Wiley Online Library for rules of use; OA articles are governed by the applicable Creative Commons License

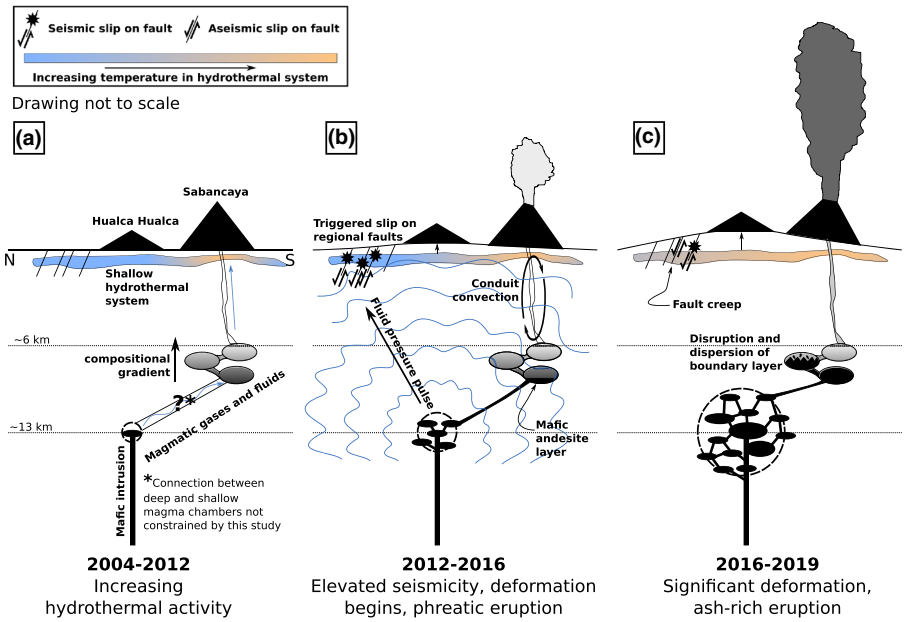

Figure 12. Conceptual model for 2012–2019 eruptive sequence at Sabancaya. See text for explanation.

First (Figure 12a), a mafic intrusion around 2011–2012 (thermal and degassing anomalies, Figure 11c) at ~13 km depth (InSAR modeled deep inflation, Figure 4) brings a fresh charge of heat and magmatic gases into the magmatic plumbing system beneath Hualca Hualca and Sabancaya, reactivating the shallow dacitic magma chamber at ~6 km depth (petrologic data, Gerbe & Thouret, 2004). Heat and magmatic gases from the dacitic magma chamber travel along preexisting permeable pathways in the volcanic conduit at Sabancaya (Moussallam et al., 2017), causing thermal anomalies and elevated degassing at Sabancaya (Figure 12a). This is consistent with the increase between 2011 and 2012 in thermal and SO_2 output at Sabancaya (Figure 11c), the depth of the best fit model for the InSAR time series (Figure 4), and the petrologic evidence for magma mixing between dacite and a mafic intrusion in the 1990–1998 eruption in Gerbe and Thouret (2004).

Second, pressure in the zone of mafic magma storage builds sufficiently to cause a stress perturbation that creates a fluid pressure pulse (e.g., White & McCausland, 2016), causing tectonic earthquakes on several regional faults (Figure 12b). These earthquakes preferentially occur to the north of Sabancaya (Figure 1c; Figure 1 of Jay et al., 2015), closer to the source of the stress perturbation (the deep inflation source, Figure 4). Deformation from the mafic intrusion begins to be detectable via InSAR (Figure 11a). We note that the intrusion rate prior to 2013 was likely low enough to be undetectable with the limited InSAR data available during this time period (Figure 11a). A layer of mafic andesite forms at the base of the shallow storage zone (mafic enclaves in tephra from 1990–1998 eruption, Gerbe & Thouret, 2004). The heat and magmatic gases from the undegassed mafic magma (e.g., Edmonds et al., 2001, 2019) drive convection in the conduit of Sabancaya (Moussallam et al., 2017), leading to a steady hydrothermal plume and phreatic eruption, consistent with sustained high temperatures between 2012 and 2016 (Figures 1a and 11c).

Finally, disruption and dispersion of the mafic andesite layer in the magma reservoir lead to higher intensity ash-rich eruptions (Figure 12c of this study, Gerbe & Thouret, 2004). Static stress from the now larger intrusion drives long-lived creep, in agreement with this study's InSAR observations of long-term aseismic slip (Figure 8) and static stress calculations (Figure S8). The sustained elevated heat flow eventually reactivates hydrothermal activity at Hualca Hualca (new thermal anomaly at Hualca Hualca in 2017; Figure 11c of this study; Macedo, 2018), leading to higher pore pressures and slip on faults in the hydrothermally active areas (Figures 3 and 10 of this study; Macedo, 2018).

This conceptual model pulls together evidence from InSAR, gas and thermal monitoring, seismic records, and petrology to explain two puzzling features of volcanic activity at Sabancaya: the inflation source that is

21699356, 2020, 5, Downloaded from https://agupubs.onlinelibrary.wiley.com/doi/10.1029/2019JB019281, Wiley Online Library on [17/06/2024]. See the Terms and Conditions (https://onlinelibrary.wiley.com/terms-and-conditions) on Wiley Online Library for rules of use; OA articles are governed by the applicable Creative Commons License

offset from the eruption in both time and space, and the strong tectonic seismicity observed during eruptive periods. A mafic intrusion at depth, centered beneath Hualca Hualca, with a more "closed" behavior (e.g., Chaussard et al., 2013) that perturbs a shallow, more "open" magma reservoir explains why eruptions at Sabancaya are accompanied by offset inflation that does not directly correspond to changes in eruptive activity at the surface.

7. Conclusion

We present an updated time series of deformation at Sabancaya volcano that captures deformation from volcanic inflation, two earthquakes, and fault creep, with the following key results:

1. InSAR-derived surface deformation times series data reveal a broad area of uplift north of Sabancaya with ongoing deformation from approximately 2013 through 2019. The best fit model for the uplift is a spherical inflation source centered 7 km NNW of Sabancaya with a depth of 13–14 km and a volume change rate of 0.04 to 0.05 $km^3\ yr^{-1}$.
2. The best fit source models for surface deformation from two earthquakes north of Sabancaya in January and April of 2017 are NW striking normal faults dipping to the NE, similar to mapped tectonic faults in the area.
3. Our surface deformation times series reveal aseismic creep on three faults NW of Sabancaya. Of these faults, the Mojopampa fault exhibits long-lived postseismic creep lasting for at least 6 years.
4. We find deformation from triggered slip on regional tectonic faults in response to large earthquakes in 1998 and 2013 in interferograms spanning these events.
5. Coulomb static stress changes from the modeled inflation source at Sabancaya are positive for the long-lived creeping fault and the two 2017 earthquakes.

We conclude that the deep-seated inflation beneath Hualca Hualca is evidence of a laterally and vertically complex magma plumbing system beneath Sabancaya and Hualca Hualca. We argue that the deep-seated inflation observed at Hualca Hualca represents mafic recharge of the system at depth, as in the model proposed by Gerbe and Thouret (2004). We further speculate that these mafic intrusions at depth destabilize the magmatic plumbing system, pushing it toward eruption.

This study represents a semiquantitative test of the "distal VTs" framework for understanding precursory seismic activity as put forward by White and McCausland (2016). We argue that the key conditions for generating large magnitude seismicity in volcanic areas are significant magmatic inflation, extensive hydrothermal activity, and offset uplift beneath an area of low heat flow that favors the formation of larger faults.

InSAR observations spanning nearly three decades, and ground and satellite observations of hydrothermal activity, are key for our conceptual model of the 2013–2019 eruption at Sabancaya. InSAR-observed triggered slips in response to large earthquakes, and satellite and ground observations of extensive hydrothermal activity around Sabancaya, support our argument for a highly fractured, fluid-saturated crust perpetually at a critical state of stress in the region around Sabancaya. In our model, the stress perturbation from a magma intrusion at 13–14 km depth, first inferred via satellite thermal and degassing anomalies in 2011–2012 and later detectable via InSAR in 2013, triggers seismicity on regional tectonic faults in 2013 via a fluid pressure pulse. As the intrusion continues from 2013 through 2019, high regional fluid pore pressures, evident through satellite and ground observations in 2017 of the reinvigorated hydrothermal system at Hualca Hualca, also facilitate creep driven by static stress transfer from the deep inflation source. Static stress transfer from the ongoing intrusion is also sufficient to promote additional seismogenic slip on faults north of Hualca Hualca.

Acknowledgments

P. G. M., K. R., and M. E. P. were partly supported by Grant NNX16AK87G issued through NASA's Science Mission Directorate's Earth Science Division. F. D. was supported by the NASA ESSF program for PhD fellowships and by a Centre National D'Etudes Spatiales (CNES) postdoctoral grant. M. B. was supported by an appointment to the NASA Postdoctoral Program at the Jet Propulsion Laboratory, administered by the Universities Space and Research Association (USRA) through a contract with NASA. We thank the Italian Space Agency (ASI) for providing COSMO-SkyMed data for this project. Original COSMO-SkyMed product ASI Agenzia Spaziale Italiana (2014–2019). CSK data were provided by an agreement between Agenzia Spaziale Italiana (ASI) and JPL. We acknowledge the CEOS volcano pilot project and the German Space Agency for TSX/TDX data from that project. The European Space Agency provided Sentinel-1, ERS-1/2, and Envisat data. F.D. acknowledges Tara Shreve (IPGP) for useful discussions. We would also like to thank the two anonymous reviewers whose detailed comments greatly improved this manuscript. Data and model files for this paper are available via the Zenodo repository (at https://zenodo.org/record/3733800).

References

Agram, P., Jolivet, R., Simons, M., & Riel, B. (2012). GIAnT,-generic InSAR analysis toolbox. In *AGU Fall Meeting Abstracts*, *43*, pp. 0897.

Albino, F., Biggs, J., & Syahbana, D. K. (2019). Dyke intrusion between neighbouring arc volcanoes responsible for 2017 pre-eruptive seismic swarm at Agung. *Nature Communications*, *10*(1), 1–11. https://doi.org/10.1038/s41467-019-08564-9

Anccasi Figueroa, R. M., Ortega Gonzáles, M. A., Ccallata Pacsi, B., & Machacca Puma, R. (2018). Actividad sísmica distal en el volcán Sabancaya (2015 - 2017). Repositorio Institucional INGEMMET.

Antayhua, Y., Tavera, H., & Bernal Esquia, I. (2001). Análisis de la actividad sísmica en la región del volcán Sabancaya (Arequipa. Repositorio institucional - IGP.

Antayhua, Y., Tavera, H., Bernal Esquia, I., Palza, H., & Aguilar, V. (2002). Localización hipocentrales y características de la fuente de los sismos de Maca (1991), Sepina (1992) y Cabanaconde (1998) Región Volcánica Sabancaya (Arequipa). Repositorio institucional - IGP.

21699356, 2020, 5, Downloaded from https://agupubs.onlinelibrary.wiley.com/doi/10.1029/2019JB019281, Wiley Online Library on [17/06/2024]. See the Terms and Conditions (https://onlinelibrary.wiley.com/terms-and-conditions) on Wiley Online Library for rules of use; OA articles are governed by the applicable Creative Commons License

Avouac, J.-P. (2015). From geodetic imaging of seismic and aseismic fault slip to dynamic modeling of the seismic cycle. *Annual Review of Earth and Planetary Sciences*, *43*(1), 233–271. https://doi.org/10.1146/annurev-earth-060614-105302

Barnhart, W. D., & Lohman, R. B. (2010). Automated fault model discretization for inversions for coseismic slip distributions. *Journal of Geophysical Research*, *115*, B10419. https://doi.org/10.1029/2010JB007545

Benavente, C., Delgado, F., Aguirre, E., Albinez, L., & Audin, L. (2016). Mapa Neotectónico Región Arequipa.

Benavente Escobar, C. L., Delgado Madera, G. F., Garcáa Fernández Baca, B., Aguirre Alegre, E. M., & Audin, L. (2018). Neotectónica, evolución del relieve y peligro sésmico en la región Arequipa - [Boletín C 64], Repositorio Institucional INGEMMET.

Berardino, P., Fornaro, G., Lanari, R., & Sansosti, E. (2002). A new algorithm for surface deformation monitoring based on small baseline differential SAR interferograms. *IEEE Transactions on Geoscience and Remote Sensing*, *40*(11), 2375–2383. https://doi.org/10.1109/TGRS.2002.803792

Bürgmann, R. (2018). The geophysics, geology and mechanics of slow fault slip. *Earth and Planetary Science Letters*, *495*, 112–134. https://doi.org/10.1016/j.epsl.2018.04.062

Byrdina, S., Ramos, D., Vandemeulebrouck, J., Masias, P., Revil, A., Finizola, A., et al. (2013). Influence of the regional topography on the remote emplacement of hydrothermal systems with examples of Ticsani, and Ubinas volcanoes, Southern. *Peru, Earth and Planetary Science Letters*, *365*, 152–164. https://doi.org/10.1016/j.epsl.2013.01.018

Carn, S. A., Fioletov, V. E., McLinden, C. A., Li, C., & Krotkov, N. A. (2017). A decade of global volcanic SO_2 emissions measured from space. *Scientific Reports*, *7*(1), 1–12. https://doi.org/10.1038/srep44095

Cashman, K., & Biggs, J. (2014). Common processes at unique volcanoes—A volcanological conundrum. *Frontiers in Earth Science*, 2. https://doi.org/10.3389/feart.2014.00028

Cashman, K. V., Sparks, R. S. J., & Blundy, J. D. (2017). Vertically extensive and unstable magmatic systems: A unified view of igneous processes. *Science*, *355*(6331), eaag3055. https://doi.org/10.1126/science.aag3055

Chadwick, W. W., Geist, D. J., Jónsson, S., Poland, M., Johnson, D. J., & Meertens, C. M. (2006). A volcano bursting at the seams: Inflation, faulting, and eruption at Sierra Negra volcano, Galápagos. *Geology*, *34*(12), 1025–1028. https://doi.org/10.1130/G22826A.1

Chaussard, E., Amelung, F., & Aoki, Y. (2013). Characterization of open and closed volcanic systems in Indonesia and Mexico using inSAR time series. *Journal of Geophysical Research: Solid Earth*, *118*, 3957–3969. https://doi.org/10.1002/jgrb.50288

Chen, C. W., & Zebker, H. A. (2001). Two-dimensional phase unwrapping with use of statistical models for cost functions in nonlinear optimization. *JOSA A*, *18*(2), 338–351. https://doi.org/10.1364/JOSAA.18.000338

Comeau, M. J., Unsworth, M. J., & Cordell, D. (2016). New constraints on the magma distribution and composition beneath volcán Uturuncu and the southern Bolivian Altiplano from magnetotelluric data. *Geosphere*, *12*(5), 1391–1421. https://doi.org/10.1130/GES01277.1

Cruz, L., Taipe Maquerhua, E. L., & Miranda Cruz, R. (2018). Asociación de la deformación registrada con GNSS CORS con las intrusiones magmáticas en el volcán Sabancaya durante el 2017, Repositorio Institucional INGEMMET.

Dalmayrac, B., & Molnar, P. (1981). Parallel thrust and normal faulting in Peru and constraints on the state of stress. *Earth and Planetary Science Letters*, *55*(3), 473–481. https://doi.org/10.1016/0012-821X(81)90174-6

Delgado, F., Pritchard, M. E., Ebmeier, S., González, P., & Lara, L. (2017). Recent unrest (2002–2015) imaged by space geodesy at the highest risk Chilean volcanoes: Villarrica, Llaima, and Calbuco (Southern Andes). *Journal of Volcanology and Geothermal Research*, *344*(Supplement C), 270–288. https://doi.org/10.1016/j.jvolgeores.2017.05.020

Delgado, F., Pritchard, M., Samsonov, S., & Córdova, L. (2018). Renewed posteruptive uplift following the 2011–2012 rhyolitic eruption of cordón Caulle (Southern Andes, Chile): Evidence for transient episodes of magma reservoir recharge during 2012–2018. *Journal of Geophysical Research: Solid Earth*, *123*, 9407–9429. https://doi.org/10.1029/2018JB016240

Devlin, S., Isacks, B. L., Pritchard, M. E., Barnhart, W. D., & Lohman, R. B. (2012). Depths and focal mechanisms of crustal earthquakes in the central Andes determined from teleseismic waveform analysis and inSAR. *Tectonics*, *31*, TC2002. https://doi.org/10.1029/2011TC002914

Ebmeier, S. K., Andrews, B. J., Araya, M. C., Arnold, D. W. D., Biggs, J., Cooper, C., et al. (2018). Synthesis of global satellite observations of magmatic and volcanic deformation: Implications for volcano monitoring & the lateral extent of magmatic domains. *Journal of Applied Volcanology*, *7*(1), 2. https://doi.org/10.1186/s13617-018-0071-3

Ebmeier, S. K., Elliott, J. R., Nocquet, J.-M., Biggs, J., Mothes, P., Jarrín, P., et al. (2016). Shallow earthquake inhibits unrest near Chiles-Cerro Negro volcanoes, Ecuador-Colombian border. *Earth and Planetary Science Letters*, *450*, 283–291. https://doi.org/10.1016/j.epsl.2016.06.046, .

Edmonds, M., Aiuppa, A., Humphreys, M., Moretti, R., Giudice, G., Martin, R. S., et al. (2010). Excess volatiles supplied by mingling of mafic magma at an andesite arc volcano. *Geochemistry, Geophysics, Geosystems*, *11*, Q04005. https://doi.org/10.1029/2009GC002781

Edmonds, M., Cashman, K. V., Holness, M., & Jackson, M. (2019). Architecture and dynamics of magma reservoirs. *Philosophical Transactions of the Royal Society A: Mathematical, Physical and Engineering Sciences*, *377*(2139), 20180298. https://doi.org/10.1098/rsta.2018.0298

Edmonds, M., Pyle, D., & Oppenheimer, C. (2001). A model for degassing at the Soufriére Hills volcano, Montserrat, West Indies, based on geochemical data. *Earth and Planetary Science Letters*, *186*(2), 159–173. https://doi.org/10.1016/S0012-821X(01)00242-4

Eichelberger, J. C., Izbekov, P. E., Francis, P., Neuberg, J., & Sparks, R. S. J. (2000). Eruption of andesite triggered by dyke injection: Contrasting cases at Karymsky Volcano, Kamchatka and Mt Katmai, Alaska. *Philosophical Transactions of the Royal Society of London. Series A: Mathematical, Physical and Engineering Sciences*, *358*(1770), 1465–1485. https://doi.org/10.1098/rsta.2000.0599

Farr, T. G., Rosen, P. A., Caro, E., Crippen, R., Duren, R., Hensley, S., et al. (2007). The Shuttle Radar Topography Mission. *Reviews of Geophysics*, *45*, RG2004. https://doi.org/10.1029/2005RG000183

Finnegan, N. J., Pritchard, M. E., Lohman, R. B., & Lundgren, P. R. (2008). Constraints on surface deformation in the Seattle, WA, urban corridor from satellite radar interferometry time-series analysis. *Geophysical Journal International*, *174*(1), 29–41. https://doi.org/10.1111/j.1365-246X.2008.03822.x

Flesch, L. M., Holt, W. E., Haines, A. J., & Shen-Tu, B. (2000). Dynamics of the Pacific-North American plate boundary in the western United States. *Science*, *287*(5454), 834–836. https://doi.org/10.1126/science.287.5454.834

Gaherty, J. B., Zheng, W., Shillington, D. J., Pritchard, M. E., Henderson, S. T., Chindandali, P. R. N., et al. (2019). Faulting processes during early-stage rifting: Seismic and geodetic analysis of the 2009–2010 northern Malawi earthquake sequence. *Geophysical Journal International*, *217*(3), 1767–1782. https://doi.org/10.1093/gji/ggz119

Gerbe, M.-C., & Thouret, J.-C. (2004). Role of magma mixing in the petrogenesis of tephra erupted during the 1990–98 explosive activity of Nevado sabancaya, southern Peru. *Bulletin of Volcanology*, *66*(6), 541–561. https://doi.org/10.1007/s00445-004-0340-3

Global Volcanism Program (1988). Report on Sabancaya (Peru) (*13:6*): Smithsonian Institution.

Global Volcanism Program (2000). Report on Sabancaya (Peru) (*25:5*): Smithsonian Institution.

21699356, 2020, 5, Downloaded from https://agupubs.onlinelibrary.wiley.com/doi/10.1029/2019JB019281, Wiley Online Library on [17/06/2024]. See the Terms and Conditions (https://onlinelibrary.wiley.com/terms-and-conditions) on Wiley Online Library for rules of use; OA articles are governed by the applicable Creative Commons License

Global Volcanism Program (2003). Report on Sabancaya (Peru) (*28*:5): Smithsonian Institution.
Global Volcanism Program (2013). Volcanoes of the World, v. 4.8.0., smithsonian Institution.
Global Volcanism Program (2016). Report on Sabancaya (Peru) (*41*:5): Smithsonian Institution.
Global Volcanism Program (2017). Report on Sabancaya (Peru) (*42*:5): Smithsonian Institution.
Goldstein, R. M., Zebker, H. A., & Werner, C. L. (1988). Satellite radar interferometry: Two-dimensional phase unwrapping. *Radio Science*, *23*(4), 713–720. https://doi.org/10.1029/RS023i004p00713
Gudmundsson, A. (2011). *Rock fractures in geological processes*. Cambridge: Cambridge University Press. https://doi.org/10.1017/CBO9780511975684
Hayes, G. P., Wald, D. J., & Johnson, R. L. (2012). Slab1.0: A three-dimensional model of global subduction zone geometries. *Journal of Geophysical Research*, *117*, B01302. https://doi.org/10.1029/2011JB008524
Heap, M. J., Villeneuve, M., Albino, F., Farquharson, J. I., Brothelande, E., Amelung, F., et al. (2019). Towards more realistic values of elastic moduli for volcano modelling. *Journal of Volcanology and Geothermal Research*, *390*, 106684. https://doi.org/10.1016/j.jvolgeores.2019.106684
Henderson, S. T., & Pritchard, M. E. (2013). Decadal volcanic deformation in the Central Andes Volcanic Zone revealed by inSAR time series. *Geochemistry, Geophysics, Geosystems*, *14*, 1358–1374. https://doi.org/10.1002/ggge.20074
Henderson, S. T., & Pritchard, M. E. (2017). Time-dependent deformation of Uturuncu volcano, Bolivia, constrained by GPS and inSAR measurements and implications for source models. *Geosphere*, *13*(6), 1–21. https://doi.org/10.1130/GES01203.1
Hickey, J., Gottsmann, J., & del Potro, R. (2013). The large-scale surface uplift in the Altiplano-Puna region of Bolivia: A parametric study of source characteristics and crustal rheology using finite element analysis. *Geochemistry, Geophysics, Geosystems*, *14*, 540–555. https://doi.org/10.1002/ggge.20057
Hickey, J., Gottsmann, J., Nakamichi, H., & Iguchi, M. (2016). Thermomechanical controls on magma supply and volcanic deformation: Application to Aira caldera, Japan. *Scientific Reports*, *6*(1), 1–10. https://doi.org/10.1038/srep32691
Holtkamp, S. G., Pritchard, M. E., & Lohman, R. B. (2011). Earthquake swarms in South America. *Geophysical Journal International*, *187*(1), 128–146. https://doi.org/10.1111/j.1365-246X.2011.05137.x
Huaman-Rodrigo, D., Chorowicz, J., Deffontaines, B., Guillande, R., & Rudant, J. (1993). Cadre structural et risques géologiques étudiés á l'aide de l'imagerie spatiale: La région du Colca (Andes du sud pérou). *BULLETIN-SOCIETE GEOLOGIQUE DE FRANCE*, *164*, 807–807.
Instituto Geofísico del Perú (2017). Investigación y monitoreo de volcanes activos en el sur del Perú. Reporte técnico especial 2016: Instituto Geofiísico del Perú Observatorio Vulcanológico del Sur.
Jay, J. A. (2014). A geophysical survey of active volcanism in the central and southern Andes (Ph.D.), Cornell University.
Jay, J. A., Delgado, F. J., Torres, J. L., Pritchard, M. E., Macedo, O., & Aguilar, V. (2015). Deformation and seismicity near Sabancaya volcano, southern Peru, from 2002 to 2015. *Geophysical Research Letters*, *42*, 2780–2788. https://doi.org/10.1002/2015GL063589
Kagan, Y. Y., & Jackson, D. D. (1991). Long-term earthquake clustering. *Geophysical Journal International*, *104*(1), 117–133. https://doi.org/10.1111/j.1365-246X.1991.tb02498.x
Kern, C., Masias, P., Apaza, F., Reath, K. A., & Platt, U. (2017). Remote measurement of high preeruptive water vapor emissions at Sabancaya volcano by passive differential optical absorption spectroscopy. *Journal of Geophysical Research: Solid Earth*, *122*, 3540–3564. https://doi.org/10.1002/2017JB014020
King, G. C. P., Stein, R. S., & Lin, J. (1994). Static stress changes and the triggering of earthquakes. *Bulletin of the Seismological Society of America*, *84*(3), 935–953.
La Femina, P. C., Connor, C. B., Hill, B. E., Strauch, W., & Saballos, J. A. (2004). Magma-tectonic interactions in Nicaragua: The 1999 seismic swarm and eruption of Cerro Negro volcano. *Journal of Volcanology and Geothermal Research*, *137*(1), 187–199. https://doi.org/10.1016/j.jvolgeores.2004.05.006
Lienkaemper, J. J., & McFarland, F. S. (2017). Long-term afterslip of the 2004 *M* 6.0 Parkfield, California, earthquake—Implications for forecasting amount and duration of afterslip on other major creeping faults. *Bulletin of the Seismological Society of America*, *107*(3), 1082–1093. https://doi.org/10.1785/0120160321, .
Lin, Y.-n. N., Simons, M., Hetland, E. A., Muse, P., & DiCaprio, C. (2010). A multiscale approach to estimating topographically correlated propagation delays in radar interferograms. *Geochemistry, Geophysics, Geosystems*, *11*, Q09002. https://doi.org/10.1029/2010GC003228
Lohman, R. B., & Simons, M. (2005). Some thoughts on the use of inSAR data to constrain models of surface deformation: Noise structure and data downsampling. *Geochemistry, Geophysics, Geosystems*, *6*, Q01007. https://doi.org/10.1029/2004GC000841
Lu, Z., & Dzurisin, D. (2014). InSAR imaging of Aleutian volcanoes. In Z. Lu, & D. Dzurisin (Eds.), *InSAR imaging of Aleutian volcanoes: Monitoring a volcanic arc from space* pp. 87–345), Springer Praxis Books. Berlin, Heidelberg: Springer. https://doi.org/10.1007/978-3-642-00348-6&urluscore;6
Lundgren, P., Nikkhoo, M., Samsonov, S. V., Milillo, P., Gil-Cruz, F., & Lazo, J. (2017). Source model for the Copahue, volcano magma plumbing system constrained by InSAR surface deformation observations. *Journal of Geophysical Research*, *122*, 5729–5747. https://doi.org/10.1002/2017JB014368
MacQueen, P., Zurek, J., & Williams-Jones, G. (2016). Connected magma plumbing system between Cerro Negro and El Hoyo Complex, Nicaragua, revealed by gravity survey. *Journal of Volcanology and Geothermal Research*, *327*(Supplement C), 375–384. https://doi.org/10.1016/j.jvolgeores.2016.09.002, .
Macedo, O. (2018). Observaciones de campo en la zona de Pinchollo al norte del volcán Sabancaya, Informe Técnico, Instituto Geofísico del Perú.
Machacca Puma, R., Ortega, M. A., Gonzáles, R., Miranda Cruz, R., Apaza Choquehuayta, F. E., Lazarte Zerpa, I. A., et al. (2018). *Monitoreo Multi-paramétrico del volcán Sabancaya y evolución del proceso eruptivo 2016–2017*. In *Libro de resúmenes: VIII Foro Internacional los Volcanes y su Impacto, Arequipa, 26 y 27 de abril del 2018*, pp. 105–108. Arequipa, Peru, Instituto Geológico Minero y Metalúrgico -INGEMMET.
Machare, J., Fenton, C. H., Machette, M. N., Lavenu, A., Costa, C., & Dart, R. L. (2003). *Database and map of Quaternary faults and folds in Peru and its offshore region*, USGS Numbered Series 2003-451: United States Geological Survey.
Manrique Llerena, N., Lazarte Zerpa, I. A., Sandoval, C., Arnold, K., Rivera Porras, M. A., & Aguilar Contreras, R. (2018). Actividad del volc'an Sabancaya (Perú) 2016–2017: Características de las emisiones de ceniza y análisis granulométrico. Libro de resúmenes: VIII Foro Internacional los Volcanes y su Impacto, Arequipa, 26 y 27 de abril del 2018.
Marco, S., Stein, M., Agnon, A., & Ron, H. (1996). Long-term earthquake clustering: A 50,000-year paleoseismic record in the Dead Sea Graben. *Journal of Geophysical Research*, *101*(B3), 6179–6191. https://doi.org/10.1029/95JB01587
McTigue, D. F. (1987). Elastic stress and deformation near a finite spherical magma body: Resolution of the point source paradox. *Journal of Geophysical Research*, *92*(B12), 12,931–12,940. https://doi.org/10.1029/JB092iB12p12931

21699356, 2020, 5, Downloaded from https://agupubs.onlinelibrary.wiley.com/doi/10.1029/2019JB019281, Wiley Online Library on [17/06/2024]. See the Terms and Conditions (https://onlinelibrary.wiley.com/terms-and-conditions) on Wiley Online Library for rules of use; OA articles are governed by the applicable Creative Commons License

Mellors, R. J., Magistrale, H., Earle, P., & Cogbill, A. (2004). Comparison of four moderate-size earthquakes in Southern California using seismology and inSAR. *Bulletin of the Seismological Society of America*, *94*(6), 2004–2014. https://doi.org/10.1785/0120020219

Mering, C., Huaman-Rodrigo, D., Chorowicz, J., Deffontaines, B., & Guillande, R. (1996). New data on the geodynamics of southern Peru from computerized analysis of SPOT and SAR ERS-1 images. *Tectonophysics*, *259*(1), 153–169. https://doi.org/10.1016/0040-1951(96)00034-0

Miller, S. A., Collettini, C., Chiaraluce, L., Cocco, M., Barchi, M., & Kaus, B. J. P. (2004). Aftershocks driven by a high-pressure CO_2 source at depth. *Nature*, *427*(6976), 724–727. https://doi.org/10.1038/nature02251

Mogi, K. (1958). Relations between the eruptions of various volcanoes and the deformations of the ground surfaces around them. *Bulletin of the Earthquake Research Institute*, *36*, 99–134.

Morales Rivera, A. M., Amelung, F., & Mothes, P. (2016). Volcano deformation survey over the northern and central Andes with ALOS inSAR time series. *Geochemistry, Geophysics, Geosystems*, *17*, 2869–2883. https://doi.org/10.1002/2016GC006393

Moussallam, Y., Tamburello, G., Peters, N., Apaza, F., Schipper, C. I., Curtis, A., et al. (2017). Volcanic gas emissions and degassing dynamics at Ubinas and Sabancaya volcanoes; implications for the volatile budget of the central volcanic zone. *Journal of Volcanology and Geothermal Research*, *343*, 181–191. https://doi.org/10.1016/j.jvolgeores.2017.06.027

Newman, A. V., Dixon, T. H., & Gourmelen, N. (2006). A four-dimensional viscoelastic deformation model for Long Valley caldera, California, between 1995 and 2000. *Journal of Volcanology and Geothermal Research*, *150*(1), 244–269. https://doi.org/10.1016/j.jvolgeores.2005.07.017

Nishimura, T., Fujiwara, S., Murakami, M., Tobita, M., Nakagawa, H., Sagiya, T., & Tada, T. (2001). The *M*6.1 earthquake triggered by volcanic inflation of Iwate volcano, northern Japan, observed by satellite radar interferometry. *Geophysical Research Letters*, *28*(4), 635–638. https://doi.org/10.1029/2000GL012022

Okada, Y. (1985). Surface deformation due to shear and tensile faults in a half-space. *Bulletin of the Seismological Society of America*, *75*(4), 1135–1154.

Perfettini, H., & Avouac, J.-P. (2004). Postseismic relaxation driven by brittle creep: A possible mechanism to reconcile geodetic measurements and the decay rate of aftershocks, application to the Chi-Chi earthquake, Taiwan. *Journal of Geophysical Research*, *109*, B02304. https://doi.org/10.1029/2003JB002488

Poland, M. P., Peltier, A., Bonforte, A., & Puglisi, G. (2017). The spectrum of persistent volcanic flank instability: A review and proposed framework based on Kilauea, Piton de la Fournaise, and Etna. *Journal of Volcanology and Geothermal Research*, *339*, 63–80. https://doi.org/10.1016/j.jvolgeores.2017.05.004

Pritchard, M. E., Biggs, J., Wauthier, C., Sansosti, E., Arnold, D. W. D., Delgado, F., et al. (2018). Towards coordinated regional multi-satellite inSAR volcano observations: Results from the Latin America pilot project. *Journal of Applied Volcanology*, *7*(1), 5. https://doi.org/10.1186/s13617-018-0074-0

Pritchard, M. E., & Simons, M. (2004). An inSAR-based survey of volcanic deformation in the central Andes. *Geochemistry, Geophysics, Geosystems*, *5*, Q02002. https://doi.org/10.1029/2003GC000610

Puma, N., Torres, J., Macedo, O., Centeno, R., Del Carpio, J., & Cruz, J. (2016). Evolución de la actividad sismo-volcánica en la zona del volcán Sabancaya (2013–2016), in XVIII Congreso Peruano de Geología. Sociedad Geologica del Perú.

Rankin, A. J. (2012). Predicted ash hazards from potential eruptions at Nevado Sabancaya, Peru: HYSPLIT and remote sensing (Master's thesis), State University of New York at Buffalo, United States—New York.

Reath, K., Pritchard, M. E., Moruzzi, S., Alcott, A., Coppola, D., & Pieri, D. (2019b). The AVTOD (ASTER Volcanic Thermal Output Database) Latin America archive. *Journal of Volcanology and Geothermal Research*, *376*, 62–74. https://doi.org/10.1016/j.jvolgeores.2019.03.019

Reath, K., Pritchard, M., Poland, M., Delgado, F., Carn, S., Coppola, D., et al. (2019a). Thermal, deformation, and degassing remote sensing time series (CE 2000–2017) at the 47 most active volcanoes in Latin America: Implications for Volcanic Systems. *Journal of Geophysical Research: Solid Earth*, *124*, 195–218. https://doi.org/10.1029/2018JB016199

Rey, P., Vanderhaeghe, O., & Teyssier, C. (2001). Gravitational collapse of the continental crust: Definition, regimes and modes. *Tectonophysics*, *342*(3), 435–449. https://doi.org/10.1016/S0040-1951(01)00174-3

Riddick, S. N., & Schmidt, D. A. (2011). Time-dependent changes in volcanic inflation rate near Three Sisters, Oregon, revealed by inSAR. *Geochemistry, Geophysics, Geosystems*, *12*, Q12005. https://doi.org/10.1029/2011GC003826

Rodríguez, A., & Uribe, M. (1994). Participación del Instituto Geofísico del Perú en relación con la reactivación del volcán Sabancaya, Provincia de Caylloma, Región Arequipa, Informe División de Sismología y Gravimetría, IGP-Arequipa.

Rosen, P. A., Gurrola, E. M., Agram, P. S., Sacco, G. F., & Lavalle, M. (2015). The InSAR Scientific Computing Environment (ISCE): A Python framework for Earth science. In *AGU Fall Meeting Abstracts*, *11*, pp. IN11C–1789.

Rosen, P. A., Hensley, S., Peltzer, G., & Simons, M. (2004). Updated repeat orbit interferometry package released, EOS. *Transactions American Geophysical Union*, *85*(5), 47–47. https://doi.org/10.1029/2004EO050004

Samaniego, P., Rivera, M., Mariño, J., Guillou, H., Liorzou, C., Zerathe, S., et al. (2016). The eruptive chronology of the Ampato-Sabancaya volcanic complex (Southern Peru). *Journal of Volcanology and Geothermal Research*, *323*, 110–128. https://doi.org/10.1016/j.jvolgeores.2016.04.038

Sambridge, M. (1999). Geophysical inversion with a neighbourhood algorithm I. Searching a parameter space. *Geophysical Journal International*, *138*(2), 479–494. https://doi.org/10.1046/j.1365-246X.1999.00876.x

Schmidt, D. A., & Bürgmann, R. (2008). Predicted reversal and recovery of surface creep on the Hayward fault following the 1906 San Francisco earthquake. *Geophysical Research Letters*, *35*, L19305. https://doi.org/10.1029/2008GL035270

Sébrier, M., Mercier, J. L., Mégard, F., Laubacher, G., & Carey-Gailhardis, E. (1985). Quaternary normal and reverse faulting and the state of stress in the central Andes of south Peru. *Tectonics*, *4*(7), 739–780. https://doi.org/10.1029/TC004i007p00739

Segall, P., & Rice, J. R. (1995). Dilatancy, compaction, and slip instability of a fluid-infiltrated fault. *Journal of Geophysical Research*, *100*(B11), 22,155–22,171. https://doi.org/10.1029/95JB02403

Selverstone, J. (2005). Are the Alps collapsing? *Annual Review of Earth and Planetary Sciences*, *33*(1), 113–132. https://doi.org/10.1146/annurev.earth.33.092203.122535

Singer, B. S., Mével, H. L., Licciardi, J. M., Córdova, L., Tikoff, B., Garibaldi, N., et al. (2018). Geomorphic expression of rapid Holocene silicic magma reservoir growth beneath Laguna del Maule, Chile. *Science Advances*, *4*(6), eaat1513. https://doi.org/10.1126/sciadv.aat1513

Stein, R. S. (1999). The role of stress transfer in earthquake occurrence. *Nature*, *402*(6762), 605–609. https://doi.org/10.1038/45144

Taipe Maquerhua, E. L., Miranda Cruz, R., & Dáaz Apaza, J. (2016). Análisis de deformación del volcán Sabancaya con datos GPS, periodo 2015, Instituto Geológico, Minero y Metalúrgico -INGEMMET.

Toda, S., & Stein, R. (2003). Toggling of seismicity by the 1997 Kagoshima earthquake couplet: A demonstration of time-dependent stress transfer. *Journal of Geophysical Research*, *108*(B12), 2567. https://doi.org/10.1029/2003JB002527

21699356, 2020, 5, Downloaded from https://agupubs.onlinelibrary.wiley.com/doi/10.1029/2019JB019281, Wiley Online Library on [17/06/2024]. See the Terms and Conditions (https://onlinelibrary.wiley.com/terms-and-conditions) on Wiley Online Library for rules of use; OA articles are governed by the applicable Creative Commons License

Venugopal, S., Moune, S., & Williams-Jones, G. (2016). Investigating the subsurface connection beneath Cerro Negro volcano and the El Hoyo complex, Nicaragua. *Journal of Volcanology and Geothermal Research*, *325*, 211–224. https://doi.org/10.1016/j.jvolgeores.2016.06.001

Walter, T. R. (2007). How a tectonic earthquake may wake up volcanoes: Stress transfer during the 1996 earthquake-eruption sequence at the Karymsky Volcanic group, kamchatka. *Earth and Planetary Science Letters*, *264*(3), 347–359. https://doi.org/10.1016/j.epsl.2007.09.006

Walter, T. R., Wang, R., Zimmer, M., Grosser, H., Lühr, B., & Ratdomopurbo, A. (2007). Volcanic activity influenced by tectonic earthquakes: Static and dynamic stress triggering at Mt. Merapi. *Geophysical Research Letters*, *34*, L05304. https://doi.org/10.1029/2006GL028710

Wang, K., Xu, X., & Fialko, Y. (2017). Improving burst alignment in TOPS interferometry with bivariate enhanced spectral diversity. *IEEE Geoscience and Remote Sensing Letters*, *14*(12), 2423–2427. https://doi.org/10.1109/LGRS.2017.2767575

Wauthier, C., Roman, D. C., & Poland, M. P. (2016). Joint analysis of geodetic and earthquake fault-plane solution data to constrain magmatic sources: A case study from Kilauea Volcano. *Earth and Planetary Science Letters*, *455*, 38–48. https://doi.org/10.1016/j.epsl.2016.09.011

Weston, J., Ferreira, A. M. G., & Funning, G. J. (2011). Global compilation of interferometric synthetic aperture radar earthquake source models: 1. Comparisons with seismic catalogs. *Journal of Geophysical Research*, *116*, B08408. https://doi.org/10.1029/2010JB008131

White, R., & McCausland, W. (2016). Volcano-tectonic earthquakes: A new tool for estimating intrusive volumes and forecasting eruptions. *Journal of Volcanology and Geothermal Research*, *309*, 139–155. https://doi.org/10.1016/j.jvolgeores.2015.10.020

Wimpenny, S., Copley, A., Benavente, C., & Aguirre, E. (2018). Extension and dynamics of the Andes inferred from the 2016 Parina (Huarichancara) earthquake. *Journal of Geophysical Research: Solid Earth*, *123*, 8198–8228. https://doi.org/10.1029/2018JB015588

Xu, G., Xu, C., Wen, Y., & Yin, Z. (2019). Coseismic and postseismic deformation of the 2016 MW 6.2 Lampa earthquake, southern Peru, Constrained by Interferometric Synthetic Aperture Radar. *Journal of Geophysical Research: Solid Earth*, *124*, 4250–4272. https://doi.org/10.1029/2018JB016572

Yang, X.-M., Davis, P. M., & Dieterich, J. H. (1988). Deformation from inflation of a dipping finite prolate spheroid in an elastic half-space as a model for volcanic stressing. *Journal of Geophysical Research*, *93*(B5), 4249–4257. https://doi.org/10.1029/JB093iB05p04249

Zobin, V. M. (2001). Seismic hazard of volcanic activity. *Journal of Volcanology and Geothermal Research*, *112*(1), 1–14. https://doi.org/10.1016/S0377-0273(01)00230-X

21699356, 2020, 5, Downloaded from https://agupubs.onlinelibrary.wiley.com/doi/10.1029/2019JB019281, Wiley Online Library on [17/06/2024]. See the Terms and Conditions (https://onlinelibrary.wiley.com/terms-and-conditions) on Wiley Online Library for rules of use; OA articles are governed by the applicable Creative Commons License